Journal of
Materials Chemistry A

Materials for energy and sustainability

Accepted Manuscript

This article can be cited before page numbers have been issued, to do this please use: M. Kim, G. Kim, J. Kim, S. H. Kim, B. Kim and J. Kim, *J. Mater. Chem. A*, 2026, DOI: 10.1039/D6TA01339B.

ROYAL SOCIETY OF CHEMISTRY

rsc.li/materials-a

View Article Online
DOI: 10.1039/D6TA01339B

ARTICLE

Diverting the use of reduced TiO_2 from a carrier of electron-hole pairs to a reservoir of Brönsted-Lewis acidic pairs for sustainable, non-optical H_2O_2 homolysis†

Received 00th January 20xx,
Accepted 00th January 20xx

DOI: 10.1039/x0xx00000x

Minsung Kim,[1a] Gyuchan Kim,[1b] Junseo Kim,[c] Sang Hoon Kim,*[ad] Byung-Hyun Kim*[be] and Jongsik Kim*[cd]

Defective TiO_2 bears intra-bandgap states (INTRA) and a valence band (VB) that host electrons and holes, respectively, upon photo-excitation, enabling $^{\bullet}OH/O_2^{\bullet-}/^1O_2$ formation via semi-conducting pathways. However, the energetic window of INTRA/VB is often narrow or mismatches with that of semi-conducting pathways, restricting $^{\bullet}OH/O_2^{\bullet-}/^1O_2$ generation. Here, TiO_2 was calcined at 300 °C (O300) and reduced at 300-600 °C (R300-R600) to tune quantities (N)/strengths (E) of Brönsted acidic (BA^--H^+) and Lewis acidic sites with coordination numbers of 5 (LA_I) or ≤4 (LA_{II}). The catalysts revealed distinct N/E values with hierarchies of $N_{LAII}<N_{LAI}<<N_{BA-H+}$ or $E_{BA-H+}<E_{LAI}\sim E_{LAII}$. Non-photonic H_2O_2 homolysis ($H_2O_2\rightarrow 2^{\bullet}OH$) proceeded via BA^--H^+/LA_{II}, yet, hinged on BA^--H^+ with E_{BA-H+} and N_{BA-H+} dictating energy barrier ($E_{BARRIER}$) and lumped collision frequency (k_{APP}'), respectively, as corroborated by H_2O_2 consumption rate ($-r_{H2O2}$) law. $-r_{H2O2}$ values of O300/R300/R600 were challenging-to-assess, thus being assessed using their initial acetaminophen degradation rates in a per-BA^--H^+ site ($-r_{ACETAMINOPHEN,\,0,\,CO2}$) or in a per-gram ($-r_{ACETAMINOPHEN,\,0}$). R600 showed the highest E_{BA-H+} and smallest N_{BA-H+}, thus yielding the lowest $E_{BARRIER}$ and lowest k_{APP}', respectively, where the former overrode the latter to achieve the highest $-r_{ACETAMINOPHEN,\,0,\,CO2}$ for R600. R600 displayed the highest resistance to deposit poisonous oligomer/$^{\bullet}OOH$ on BA^--H^+/LA_{II} or poisonous O_2 on LA_I due to its smallest N_{BA-H+}/highest E_{BA-H+}/highest E_{LAII} for oligomer/$^{\bullet}OOH$ and the smallest N_{LAI}/highest E_{LAI} for O_2, as also substantiated by density functional theory calculations. Consequently, $-r_{ACETAMINOPHEN,\,0}$ values of R600 were higher than those of O300/R300 throughout acetaminophen decomposition recycle runs, whereas R600 was moderately recovered upon regeneration. $-r_{POLLUTANT,\,0,\,CO2}$ values of R600 were 2-23-fold and 3-10-fold higher than those of O300/R300 and ZrO_2/UiO-66, respectively, in disintegration of diverse aqueous pollutants (analgesic/endocrine disruptor/pesticide/antibiotic).

Introduction

Titanium (Ti; [Ar] $3d^2\,4s^2$) readily donates four electrons (e^-) to two oxygens (O; [He] $2s^2\,2p^4$) under oxidative conditions.[1, 2] This results in the crystallization of TiO_2 polymorphs such as *tetragonal* anatase, *tetragonal* rutile, or *orthorhombic* brookite, either of which consists of *octahedral* $[Ti^{4+}\text{-}(O^{2-})_6]^{8-}$ sub-units.[3] The Ti^{4+} cation of $[Ti^{4+}\text{-}(O^{2-})_6]^{8-}$ is *hexa*-fold coordinated by O^{2-} anions and lacks e^- in its valence $3d/4s$ sub-shells, thereby rendering it to be inaccessible to e^--ample molecules.[1, 3-5] These make Ti^{4+} bind rigidly with O^{2-} and reveal high resistance to e^- gain/loss or leaching for TiO_2 even upon its exposure to severe redox environments.[6-8] TiO_2 also imparts a characteristic band structure, whose conduction band (CB) and valence band (VB) comprise Ti^{4+} cations and O^{2-} anions, respectively. TiO_2 unveils the bandgap energy (E_g) defined by the energetic difference between the CB and VB edges (E_{CB}-E_{VB}) of 3.0-3.2 eV.[9-11] TiO_2 thereby needs ultraviolet (UV; ≥3.1 eV) for its photo-excitation, wherein e^- can migrate from the VB to the CB, generating CB electrons (e^-_{CB}) and VB holes (h^+_{VB}). These e^-_{CB}/h^+_{VB} pairs trigger semi-conducting mechanisms that yield H^+, H_2O_2, $^{\bullet}OH$, $O_2^{\bullet-}$, or $^1O_2$ via e^- donation/withdrawal, under aqueous phases (Table S1†). Among these, $^{\bullet}OH$ outcompetes $O_2^{\bullet-}/^1O_2$ in destabilizing refractory toxicants, as proved by redox potentials (E_{REDOX}) of ~2.7 V for $^{\bullet}OH$ and ≤~2.2 V for $O_2^{\bullet-}/^1O_2$.[9, 10, 12-18]

Albeit with the marked oxophilicity of TiO_2, it consists of O-Ti^{4+}-O-Ti^{4+} channels, a fraction of which are surface-terminated and facilitate the release of oxygen ($1/2O_2$) via O-Ti^{4+}-O-$Ti^{4+}\rightarrow$O-$\bullet Ti^{4+}$-O_V-$\bullet Ti^{4+}$+$1/2O_2\rightarrow O_V$-$\bullet Ti^{4+}\bullet$-O_V-$\bullet Ti^{4+}$+O_2 or the formation of labile oxygen ($^{\bullet}O_L$) dangling to Ti^{4+} via O-Ti^{4+}-O-$Ti^{4+}\rightarrow$O-$\bullet Ti^{4+}$-O_V-Ti^{4+}-$^{\bullet}O_L$ (*-***; Fig. 1A/1C). These processes also involve the

[a] Extreme Materials Research Center, Korea Institute of Science and Technology, Seoul, 02792, South Korea.
[b] Department of Applied Chemistry, Center for Bionano Intelligence Education and Research, Hanyang ~~Univeristy~~ University ERICA, Ansan, 15588, South Korea.
[c] Department of Chemical Engineering (Integrated Engineering Program), Kyung Hee University, Yongin, 17104, South Korea.
[d] KHU-KIST Department of Converging Science and Technology, Kyung Hee University, Seoul, 02447, South Korea.
[e] Department of Energy and Bio Sciences, Hanyang ~~Univeristy~~ University ERICA, Ansan, 15588, South Korea.
[1] Co-1st authors.
* Co-corresponding authors: kim_sh@kist.re.kr (S. H. Kim); bhkim00@hanyang.ac.kr (B.-H. Kim); jkim40@khu.ac.kr (J. Kim).
† Supplementary Information available: Experimental and computational sections; Semi-conducting mechanisms; Secondary quenching rate constants for the scavengers; Ionization potentials for the aqueous toxicants; Properties, surfaces, Tauc fits, XRD patterns, Raman/XP/EPR spectra, N_2/CO/CO_2 isotherms, and CO-TPD/CO_2-TPD profiles for the (used) catalysts; Reaction profiles, rates, k_{APP} values, Arrhenius plots, rate laws, and toxicant degradation pathways for the (used) catalysts. See DOI: 10.1039/x0xx00000x

View Article Online DOI: 10.1039/D6TA04370B

generation of oxygen vacancies (O_V) adjacent to Lewis acidic Ti^{4+} defects with coordination number of 5 ($\bullet Ti^{4+}$; LA_I) or ≤4 ($\bullet Ti^{4+}\bullet$; LA_{II}).[19-22] Notably, LA_I and LA_{II} sites trap e^- ($\bullet$) in proximity in lieu of filling their empty 3*d*/4*s* sub-shells with e^- ($\bullet$), indicating e^- ($\bullet$) can be delocalized across the CB.[1, 19-24] However, when O_V sites are bountiful on the TiO_2 surface, intra-bandgap state can be formed between the CB and VB, while localizing e^- on the intra-bandgap state (e^-_{INTRA}) with energy of E_{INTRA}.[23-26] This reduces the energy required to commence semi-conducting mechanisms from E_g (e^-_{CB}/h^+_{VB} in defect-less TiO_2) to E_{INTRA}-E_{VB} (e^-_{INTRA}/h^+_{VB} in defective TiO_2).[23-26] In some cases, E_{INTRA}-E_{VB} is lower than the UV threshold (≥3.1 eV), thereby prompting the production of e^-_{INTRA}/h^+_{VB} pairs under visible light irradiation (<3.1 eV) and accelerating semi-conducting pathways.[23-26]

Nonetheless, photo-excitation of defective TiO_2 polymorphs using low-energy light sources remains challenging for several reasons. First, O_V formation energies (E_{OV}) of TiO_2 polymorphs increase in the sequence of anatase (~4.4 eV)<brookite (~5.2 eV)<rutile (~5.6 eV), as assessed via density-functional theory (DFT) calculations.[27] In this context, anatase can be most suitable to afford plentiful O_V (or LA_I/LA_{II}) sites on the surface, yet, can readily undergo reductive transition to rutile at ≥700 °C, unless the rutile is stabilized in amorphous or nano-scale forms .[27, 28] Second, E_{INTRA} and E_{VB} of defective TiO_2 immersed in aqueous media can be sensitive to pH values or quantities of aqueous species vicinal to TiO_2. These can also alter the E_{REDOX} values of semi-conducting pathways, which should lie between E_{INTRA} and E_{VB} for optical activation.[29-31] Indeed, it is inherently challenging to fine-tune E_{INTRA}, E_{VB}, and E_{REDOX} for selective acceleration of semi-conducting pathways on defective TiO_2 via aqueous photo-excitation.[29-31] Moreover, reduction of E_{INTRA}-E_{VB} of defective TiO_2 can elevate productivities of e^-_{INTRA}/h^+_{VB} pairs under visible light, yet, simultaneously narrows the optical energy window, thereby limiting the range of semi-conducting pathways that can be activated.[23-26, 29-31]

The limitations of semi-conducting mechanisms stated earlier motivate the use of O_V (LA_I/LA_{II}) to prompt $^\bullet$OH generation on defective TiO_2 in non-optical route, H_2O_2 homolysis, in particular (*vide infra*). Albeit it is arduous to significantly increase LA_I/LA_{II} quantities on defective TiO_2 surface, LA_I and LA_{II} can serve as anchoring spots for oxygenated species with unpaired e^- ($^\bullet$OH or $^\bullet$OOH) via covalent interactions and those with unpaired e^- or lone e^- pair ($^\bullet$OH/$^\bullet$OOH or H_2O/H_2O_2) via covalent or coordinate interactions, respectively (ii and iii; Fig. 1D).[19-22] Compared with LA_{II} sites, LA_I counterparts are more prevalent on defective TiO_2 surface due to strong oxophilicity for Ti, indicating $N_{LAII}<N_{LAI}$.[9, 10] LA_{II} sites can homolytically cleave surface-wandering, plentiful H_2O to yield $H^\bullet$ and $^\bullet$OH with the former and the latter binding with $^\bullet O_L$ and LA_I/LA_{II}, respectively, to form abundant Brönsted acidic -OH groups (BA^--H^+; ****; Fig. 1A/1C).[19-22] Consequently, the amount of BA^--H^+ sites can be far larger than those of LA_I/LA_{II} counterparts ($N_{LAII}<N_{LAI}<<N_{BA\text{-}H+}$).[9, 10, 19-22] Defective TiO_2 can then undergo thermal H_2 reduction, where BA^--H^+ bound to LA_I (or LA_{II}) can be lost via $H^\bullet$-assisted dehydration to recover LA_I (or LA_{II}), whereas O located in the middle of two Ti^{4+} for O-Ti^{4+}-O-Ti^{4+} can be consumed via $2H^\bullet$-assisted dehydration to evolve additional LA_I/LA_{II} (*****; Fig. 1C).[19-22] Hypothetically, thermal H_2 reduction can help increase the number of LA_I (or LA_{II}) species at the expense of the decrease in that of BA^--H^+ sites. Nevertheless, the hierarchy of $N_{LAII}<N_{LAI}<<N_{BA\text{-}H+}$ is likely to be preserved, given comparatively larger population of BA^--H^+ sites relative to those of LA_I/LA_{II} species, as reported previously (hypothesis I; $N_{LAI}\uparrow$, $N_{LAII}\uparrow$, $N_{BA\text{-}H+}\downarrow$, and $N_{LAII}<N_{LAI}<<N_{BA\text{-}H+}$ via H_2 reduction).[19-22]

Meanwhile, the $[Ti^{4+}\text{-}(O^{2-})_6]^{8-}$ units in TiO_2 can undergo thermal H_2 reduction, where terminal O^{2-} species are removed via H^+-mediated dehydration and generate O_V sites. This converts Ti^{4+} centers into open LA_I/LA_{II} sites ($N_{LAI}\uparrow$ and $N_{LAII}\uparrow$), whereas Ti^{4+} centers move toward O^{2-} anions positioned at the opposite sides of O_V sites, and shorten the Ti^{4+}-O^{2-} bond lengths ($d_{Ti\text{-}O}\downarrow$) to compensate for e^- loss triggered by O^{2-} removal (*****; Fig. 1B).[25] These structural changes suggest thermal H_2 reduction can elevate Lewis acidic strengths (e^- deficiency) of LA_I and LA_{II} sites (hypothesis II; $E_{LAI}\uparrow$ and $E_{LAII}\uparrow$ via H_2 reduction), whose magnitude can further increase when LA_I and LA_{II} sites are positioned on kinks rather than on ledges/terraces at higher H_2 reduction temperatures ($T_{REDUCTION}$), as reported previously.[19-22, 25, 32, 33] Concomitantly, the four equatorial O^{2-} anions vicinal to the open Ti^{4+} center move toward O_V to sterically minimize e^- repulsion (Fig. 1B), leading to distortion of the $[Ti^{4+}\text{-}(O^{2-})_6]^{8-}$ that facilitates e^- migration from O^{2-} to open Ti^{4+} center.[19-22, 25] Notably, O^{2-} anions can function as conjugate bases of BA^--H^+ sites (BA^-) inclined to bind with surface-roaming H^+ species.[19-22] In this context, it is sound that O^{2-} (BA^-) can be less nucleophilic and more vulnerable to H^+ loss ($N_{BA\text{-}H+}\downarrow$) post O_V inclusion in the $[Ti^{4+}\text{-}(O^{2-})_6]^{8-}$ distorted via thermal H_2 reduction (hypothesis III; Brönsted acidic strength of BA^--H^+ ($E_{BA\text{-}H+}$)↑ via H_2 reduction).[19-22, 25] Overall, hypotheses I-III boost the claim that thermal H_2 reduction can modulate the defective TiO_2 surface conducive to activate non-optical H_2O_2 homolysis ($H_2O_2\rightarrow 2^\bullet$OH) on LA_{II}/BA^--H^+ pairs via the elementary steps proposed below.[19-22]

Two BA^--H^+ sites can exothermically adsorb H_2O_2 via the formation of two hydrogen-bonds between BA^- species of BA^--H^+ sites and the H atoms of H_2O_2 (i; Fig. 1D).[19-22] This suggests that H_2O_2 can interact preferentially with BA^--H^+ sites rather than with LA_{II} counterparts on account of $E_{BA\text{-}H+}<E_{LAII}$ (hypothesis IV).[19-22] One O atom of the H_2O_2 bound to two BA^--H^+ can then endothermically coordinate to a LA_{II} via distortion of the H_2O_2 geometry. This interaction is more pronounced at a higher E_{LAII} due to greater intimacy between LA_{II} with the lone e^- pair of H_2O_2 (i and ii; Fig. 1D).[19-22] Afterward, the remaining O atom of H_2O_2 bound to two BA^--H^+/LA_{II} undergoes coordination to another adjacent LA_{II}, highlighting the significance of LA_{II} sites adjacent to two BA^--H^+ species.[19-22] The H_2O_2 bound to two BA^--H^+ and two LA_{II} sites experiences exothermic dissection into two $^\bullet$OH radicals, whose O atoms are covalent-bonded to LA_{II} sites, whereas H atoms are hydrogen-bonded to BA^- species of BA^--H^+ sites (i and iii; Fig. 1D).[19-22] Endothermic $^\bullet$OH desorption can be expedited at a higher $E_{BA\text{-}H+}$ or a higher E_{LAII}, where $E_{BA\text{-}H+}<E_{LAII}$ permits the speculation that detachment of $^\bullet$OH from LA_{II} is energetically more favorable than that from BA^--H^+.[19-22] This leaves $^\bullet$OH desorption from BA^--H^+ as the rate-determining step (RDS) of H_2O_2 homolysis (hypothesis V).[19-22] The energy barrier

($E_{BARRIER}$) of the RDS can be lower at a higher $E_{BA^-H^+}$, whose achievement is of high likelihood on defective TiO_2 subjected to thermal H_2 reduction, as speculated in hypothesis III.[19-22] This makes it compelling that BA^--H^+, rather than LA_{II}, is the prime active site of H_2O_2 homolysis (hypothesis VI). The lumped collision frequency (k_{APP}') can be higher at a greater $N_{BA^-H^+}$, suggesting that an optimum $T_{REDUCTION}$ is required to balance $E_{BARRIER}$ (or $E_{BA^-H^+}$) and k_{APP}' (or $N_{BA^-H^+}$) for maximizing $^\bullet$OH productivity on defective TiO_2.[19-22]

Notably, $^\bullet$OH adsorbed on BA^--H^+/LA_{II} can react with nearby H_2O_2 to release H_2O and generate $^\bullet$OOH bound to BA^--H^+/LA_{II} (poison I; Fig. 8A). Some of the $^\bullet$OOH species can deprotonate at pH values of ≥4.8 to yield $O_2^{\bullet-}$ analogues bound to LA_{II} sites (poison II; Fig. 8A).[21, 34] In addition, two vicinal $\bullet Ti^{4+}$ sites (LA_I; O_V-$\bullet Ti^{4+}$-O-$\bullet Ti^{4+}$) on defective TiO_2 surface can also interact with H_2O_2, release two $H^\bullet$ species, and evolve O_2 with two O atoms sharing e^- with two LA_I sites via the formation of covalent bonds (poison III; Fig. 8A).[34-36] Poison I-III can scarcely be desorbed from $^\bullet$OH generators (BA^--H^+/LA_{II}) or LA_I under certain conditions: a lower $E_{BA^-H^+}$ or a lower E_{LAII} retains poison I, a higher E_{LAII} stabilizes poison II, and a lower E_{LAI} persists poison III.[21] The relative abundance of N_{LAII}<N_{LAI} can further exacerbate the poison issue because LA_I clusters adjacent to LA_{II} species can sterically hamper the latter to bind with H_2O_2, thus supressing the H_2O_2 distortion and cleavage steps needed for H_2O_2 homolysis (ii-iii; Fig. 1D). Again, $^\bullet$OH is highly effective in degrading aqueous organics via addition or $H^\bullet$ abstraction, either of which, however, facilitates the production of oligomeric by-products. Such oligomers often contain e^--donating groups (*e.g.*, -OH, -NH_2, or -NH) that bind strongly with $N_{BA^-H^+}$ or LA_{II} sites at a higher $E_{BA^-H^+}$ or a higher E_{LAII}, in particular.[21, 37-39] All of these are combined to highlight the centrality of $T_{REDUCTION}$ optimization for defective TiO_2 to minimize the formation and deposition of Ti-peroxy species (poison I-III) and oligomers on $^\bullet$OH producers (BA^--H^+/LA_{II}) or LA_I.

This study targets to reframe H_2 reduction-subjected, defective TiO_2 as a reservoir of BA^--H^+/LA_{II} pairs, not a carrier of e^-_{INTRA}/h^+_{VB} pairs, where the former and the latter act as $^\bullet$OH evolvers in the absence and the presence of low-energy light, respectively. To this end, TiO_2 catalysts were synthesized oxidatively at 300 °C or reductively at 300-600 °C. Their morphological, textural, crystallographic, band-structural, electronic, and acidic features were systematically inspected via microscopy, spectroscopy, isotherm, and chemisorption techniques, some of which were complemented by DFT calculations. The catalysts were further examined via mechanistic and kinetic analysis under controlled conditions. Their activities ($E_{BARRIER}$/k_{APP}'), reusabilities (poison resistance), or adaptabilities in degrading diverse model organics such as analgesic, antibiotic, pesticide, or endocrine disruptor were explored rigorously to identify the optimal $T_{REDUCTION}$ for defective TiO_2 and the formulation of a rate law for H_2O_2 homolysis that has sparsely been elaborated to-date.

Results and discussion

Generic traits of the catalysts

$TiO(SO_4)$ and urea ($CO(NH_2)_2$) were dissolved in an aqueous medium for use as precursors of Ti^{4+} and $NH_3\bullet H_2O$, respectively. The latter was generated via urea pyrolysis under reflux and subsequently interacted with Ti^{4+} to precipitate $TiO_2\bullet H_2O$ ($TiO(OH)_2$; Fig. 1A).[40, 41] The $TiO_2\bullet H_2O$ surface could contain O-Ti^{4+}-O-Ti^{4+} channels inclined to termination assisted by NH_3 release from $NH_3\bullet H_2O$, resulting in the formation of LA_I/LA_{II}/$\bullet O_L$ species (*-***; Fig. 1C).[40, 41] $TiO_2\bullet H_2O$ then transformed into R300-R600 via exposure to reductive conditions at 300-600 °C, where $H^\bullet$/$^\bullet$OH produced from H_2O homolysis and H_2 supplied could compete in modulating $N_{BA^-H^+}$/N_{LAI} (or N_{LAII}) such as $N_{BA^-H^+}\uparrow$/N_{LAI} (or N_{LAII})$\downarrow$ for $H^\bullet$/$^\bullet$OH (****; Fig. 1A/1C) and $N_{BA^-H^+}\downarrow$/N_{LAI} (or N_{LAII})$\uparrow$ for H_2 (*****; Fig. 1B/1C).[19-22] The temperature range of 300-600 °C were chosen because anatase with the lowest E_{OV} among TiO_2 polymorphs began to crystallize at 300 °C and remained stable without transition to rutile at ≤600 °C (not shown). For comparison, $TiO_2\bullet H_2O$ was also converted to O300 via exposure to oxidative environments at 300 °C ($T_{OXIDATION}$), where H_2O could dissociate into $H^\bullet$ and $^\bullet$OH with the former being covalent-bonded with $\bullet O_L$ and the latter being anchored on LA_I/LA_{II}, tentatively leading to $N_{BA^-H^+}\uparrow$/N_{LAI} (or N_{LAII})$\downarrow$ (****; Fig. 1A/1C).[19-22] O300 thus served as a reference to disclose the merits of R300–R600 in accelerating H_2O_2 homolysis (*vide infra*).

To ensure that the catalysts should not be activated optically under visible light (<3.1 eV), these were subjected to diffuse reflectance ultraviolet-visible (UV-Vis) spectroscopy experiments. Plots of $(F(R_\infty)\bullet h\nu)^{1/2}$ *versus* $h\nu$ were constructed for the catalysts with $F(R_\infty)$, h, and ν corresponding to the reflectance of the catalyst, the Planck constant, and the frequency of photon, respectively (Fig. S1† and Eqn. S1†).[42-44] The plots were thereafter analyzed using Tauc fits, whose X-intercepts correspond to the E_g values of the catalysts (3.1-3.3 eV). These E_g values were comparable to those reported for TiO_2 polymorphs (Table S2†).[9, 10, 42-45] The results indicated that the catalysts could hardly generate e^-_{CB}/h^+_{VB} pairs used to activate semi-conducting pathways with visible light being incident. This also proved the catalysts contained only a limited number of O_V (or LA_I/LA_{II}) sites that were insufficient to generate abundant intra-bandgap states. Indeed, the catalysts could barely localize e^- on the intra-bandgap states under ambient conditions.[23-26]

Morphological and surface structural features of the catalysts were explored using their high-resolution transmission electron microscopy (HRTEM) images (Fig. 2A-2E). The images showed TiO_2 congregates with sizes of ≤50 nm and lattice fringes with d spacings ($d_{LATTICE}$) of 0.35 nm, corresponding to the surface (101) facet of *tetragonal* anatase. This was consistent with the bulk crystallographic traits of the catalysts examined using their XRD patterns, where all the bulk diffractions were indexed to those of *tetragonal* anatase (Fig. S2†). Notably, the HRTEM images of the catalysts also bore bunched dark spots near local lattice dislocations (Fig. S3†). These were attributed to dark e^--rich domains that can readily adsorb light, highly suggesting the presence of O_V sites in proximity to LA_I/LA_{II} sites or $\bullet O_L$/BA^--H^+ species used to activate H_2O_2 homolysis.[46-48] Overall, albeit with

View Article Online
DOI: 10.1039/D6TA01570B

the challenge of sufficient O_V (or LA_I/LA_{II}) production on the catalyst surfaces (Tauc fits; Fig. S1†), the catalysts (anatase) still provided a higher propensity to bear defective LA_I/LA_{II} sites in comparison with brookite/rutile under O_2 calcination or H_2 reduction environments, as conjectured given E_{OV} values reported for TiO_2 polymorphs.[27]

Meanwhile, TiO_2 crystallite sizes ($d_{CRYSTALLITE}$) of the catalysts on the bulk (101) or (200) facets were evaluated using the Scherrer equation (Table S2† and Eqn. S2†). The $d_{CRYSTALLITE}$ values increased in the sequence of O300~R300~R400 (~6.3 nm)<R500 (~7.8 nm)<R600 (~14.7 nm), indicating noticeable aggregation of TiO_2 particulates pertaining to R500 and R600.[49, 50] This was in line with the textural features of the catalysts inspected using their type IV N_2 isotherms (Fig. S4† and Table S2†). The N_2-accessible Brunauer-Emmett-Teller surface areas (S_{BET}) increased in the order of R600 (~35 m^2 g_{CAT}^{-1})<R500 (~170 m^2 g_{CAT}^{-1})<R400 (~210 m^2 g_{CAT}^{-1})<R300~O300 (~250 m^2 g_{CAT}^{-1}), whereas their N_2-accessible Barrett-Joyner-Halenda pore volumes remained similar (0.1-0.2 cm^3 g_{CAT}^{-1}). The $d_{CRYSTALLITE}/S_{BET}$ values of the catalysts suggested that the congregation of H_2-exposed TiO_2 poly-crystallites at ≥500 °C could markedly reduce $N_{BA-H+}/N_{LAI}/N_{LAII}$ of R500 and R600 and therefore should be deemed as considerable as H_2O homolysis-induced $H^{\bullet}/^{\bullet}OH$ and H_2 treatment in varying their $N_{BA-H+}/N_{LAI}/N_{LAII}$.

Interestingly, the catalysts (anatase) are terminated on the primary bulk (004) and (200) facets identified in their XRD patterns, leading to exposure of the surfaces abundant with LA_{II} sites with coordination numbers of 3-4 that were accessible to $H_2O_2/^{\bullet}OH/^{\bullet}OOH/O_2^{\bullet-}$ (Fig. S5†). If this held true, shifts in $d_{LATTICE}$ values or 2θ values of major bulk diffractions should be seen in HRTEM images and XRD patterns of the catalysts, respectively, yet, were verified not to be so. This suggested that LA_I/LA_{II} formation could incur only short-range distortions in the TiO_2 lattice ($[Ti^{4+}\text{-}(O^{2-})_6]^{8-}$ units).[1] In this sense, the catalysts were analyzed via Raman spectroscopy to further inspect their LA_I/LA_{II} properties or those associated, where N_{LAI}/N_{LAII} could be smaller at a lower S_{BET}, a longer d_{Ti-O}, or a greater $d_{CRYSTALLITE}$.[25] The Raman spectra were curve-fitted to unveil five characteristic bands indexed to either E_g or A_{1g}/B_{1g} modes (Fig. 2F-2J and Table S3†), resulting from Raman-excited stretching vibrations of defective O-Ti^{4+}-O-Ti^{4+} channels along the *a*-axis for E_g and along the *c*-axis for A_{1g}/B_{1g}.[51, 52] Notably, it was reported that Raman-unscattered photons could be confined in LA_I/LA_{II}-proximal O_V sites and enabled to broaden the E_g bands centered at Raman shifts of 146-151 cm^{-1} to greater extent if the quantity of photons trapped in O_V sites were larger.[53, 54] In this regard, full width at half the maximum intensities (FWHM) of the E_g bands served to gauge their broadness and were found to increase in the sequence of R600~R500 (~16.6 cm^{-1})<R400 (~18.6 cm^{-1})<R300~O300 (~21.3 cm^{-1}). This paralleled the trend on S_{BET} values of R600<R500<R400<R300~O300, suggesting the increase in their N_{LAI}/N_{LAII} of R600~R500<R400<R300~O300.[53, 54] Meanwhile, the E_g bands were red-shifted with the increase in $T_{REDUCTION}$ from ~151 cm^{-1} at 300-400 °C, ~149 cm^{-1} at 500 °C to ~146 cm^{-1} at 600 °C.[51, 52] These shifts indicated the photon energy required for defective O-Ti^{4+}-O-Ti^{4+} vibration increased in the order of R600<R500<R400~R300~O300. This could originate from the increase in the d_{Ti-O} values for the catalysts mediated by a decrease in N_{LAI}/N_{LAII} with the elevation of $T_{REDUCTION}$. This trend matched that on $d_{CRYSTALLITE}$ values of O300~R300~R400<R500<R600.[25] This proved TiO_2 aggregation ($N_{BA-H+}\downarrow$; $N_{LAI}/N_{LAII}\downarrow$) could override the competing effects of H_2O homolysis-induced $H^{\bullet}/^{\bullet}OH$ ($N_{BA-H+}\uparrow$; $N_{LAI}/N_{LAII}\downarrow$) and H_2 treatment ($N_{BA-H+}\downarrow$; $N_{LAI}/N_{LAII}\uparrow$) in varying $N_{BA-H+}/N_{LAI}/N_{LAII}$ of the catalysts subjected to H_2 reduction at ≥500 °C. Overall, the Raman spectral results substantiated that $N_{BA-H+}/N_{LAI}/N_{LAII}$ of R500 and R600 could be significantly smaller than those of O300, R300, and R400.

Acidic traits of the catalysts: XP and EPR spectroscopy

Surface elemental features of the catalysts were examined using X-ray photoelectron (XP) spectroscopy. Again, the catalyst surfaces comprised defective O-Ti^{4+}-O-Ti^{4+} channels, where e^- trapped in LA_I/LA_{II} sites (defective $\bullet Ti^{4+}/Ti^{4+}\bullet$ with coordination numbers of 5/≤4) cannot occupy the empty 3*d*/4*s* sub-shells of LA_I/LA_{II} or alter their formal oxidation states (+4), unless the electrophilicities of LA_I/LA_{II} (E_{LAI}/E_{LAII}) are sufficiently high.[1, 19-24] In this sense, the XP spectra of the surfaces in the Ti 2p domains were curve-fitted to unveil two sub-bands (Fig. 3A and Table S4†).[55, 56] These could be assigned to Ti^{4+} species with binding energies centered at 464.9-465.4 eV and 459.2-459.7 eV in the Ti $2p_{1/2}$ and in the Ti $2p_{3/2}$ regimes, respectively. These binding energies reflected the combined influence of N_{LAI}/N_{LAII} and E_{LAI}/E_{LAII} for defective $\bullet Ti^{4+}/Ti^{4+}\bullet$ ($N_{LAI}/N_{LAII}\uparrow$; $E_{LAI}/E_{LAII}\uparrow\rightarrow Ti^{4+}$ binding energy↑).[55, 56] The binding energies of Ti^{4+} species for O300 were 0.5 eV lower than those for R300 (*e.g.*, 459.2 eV for O300; 459.7 eV for R300 in the Ti $2p_{3/2}$ regions), suggesting N_{LAI}/N_{LAII} or E_{LAI}/E_{LAII} could be higher in R300 than in O300. However, considering that O300 and R300 were similar with regard to Raman spectral parameters of E_g and FWHM used to gauge their N_{LAI}/N_{LAII}, it was reasonable to conclude that E_{LAI}/E_{LAII} of R300 were higher than those of O300 (N_{LAI}/N_{LAII} of O300~R300; E_{LAI}/E_{LAII} of O300<R300). This proved hypothesis II ($E_{LAI}\uparrow$ and $E_{LAII}\uparrow$ via H_2 reduction). Moreover, binding energies of Ti^{4+} species were invariant across the catalysts subjected to H_2 reduction at 300-600 °C (*e.g.*, 459.7 eV for R300-R600 in the Ti $2p_{3/2}$ regions). This was coupled with the trends on E_g/FWHM (or N_{LAI}/N_{LAII}) for R300-R600 to permit N_{LAI}/N_{LAII} hierarchy of R600<R500<R400<R300 and E_{LAI}/E_{LAII} hierarchy of R300<R400<R500<R600, where the former could be offset by the latter to induce similar binding energies of Ti^{4+} species for R300-R600.

To further explore the trends on N_{LAI}/N_{LAII}, E_{LAI}/E_{LAII}, and N_{BA-H+}/E_{BA-H+} for the catalysts, their XP spectra in the O 1s regimes were curve-fitted into three sub-bands (Fig. 3B and Table S4†).[57, 58] These could be indexed to lattice O ($O_{LATTICE}$) and O of H_2O chemisorbed on LA_I/LA_{II} via the formation of pseudo-covalent/coordinative bonds ($O_{CHEMISORBED}$) with binding energies centered at 530.4-530.9 eV and 532.4-532.9 eV, respectively, in conjunction with O of $BA^-\text{-}H^+$ ($O_{BRÖNSTED}$) with binding energies centered at 530.8-531.8 eV.[57-60] Notably, both $O_{LATTICE}$ and $O_{CHEMISORBED}$ could donate e^- to nearby LA_I/LA_{II} sites ($\bullet Ti^{4+}/Ti^{4+}\bullet$) more vigorously at larger N_{LAI}/N_{LAII} or at higher

View Article Online DOI: 10.1039/D6TA01339B

E_{LAI}/E_{LAI} (N_{LAI}/N_{LAII}↑; E_{LAI}/E_{LAII}↑→$O_{LATTICE}/O_{CHEMISORBED}$ binding energies↑).[25] Again, the trend on N_{LAI}/N_{LAII} of R300-R600 (R600<R500<R400<R300) was opposite to that on their E_{LAI}/E_{LAII} (R300<R400<R500<R600), potentially resulting in comparable binding energies for $O_{LATTICE}$ and $O_{CHEMISORBED}$ species across R300-R600. Moreover, despite N_{LAI}/N_{LAII} of R300 were similar to those of O300, E_{LAI}/E_{LAII} of the former were higher than those of O300. These potentially rendered binging energy (e^- deficiency) of $O_{LATTICE}$ or $O_{CHEMISORBED}$ to be higher in R300 than in O300. Apparently, binding energies of $O_{LATTICE}$ and $O_{CHEMISORBED}$ for O300 were 530. 4 eV and 532.4 eV, respectively, both of which were 0.4-0.5 eV lower than those for R300-R600. These could support the combined trends on N_{LAI}/N_{LAII} (R600<R500<R400<R300~O300) and E_{LAI}/E_{LAII} (O300<R300<R400<R500<R600) for the catalysts, with the former being further refined with the trend on N_{LAI}/N_{LAII} assessed using $O_{CHEMISORBED}$ contents (R600<R500<R400~R300~O300).

To further inspect e^- affinity (E_{LAI}/E_{LAII}) of the catalysts, electron paramagnetic resonance (EPR) spectroscopy experiments were performed at 10 K on the catalysts being selected: O300 with the lowest E_{LAI}/E_{LAII} among the catalysts, R300 with the lowest E_{LAI}/E_{LAII} among R300-R600, and R600 with the highest E_{LAI}/E_{LAII} among the catalysts (Fig. 3C). The EPR spectra displayed signals centered at *g*-factors of 2.00, which could stem from e^- delocalized on the CB or weakly localized at O_V-proximal $•Ti^{4+}/•Ti^{4+}•$ sites (LA_I/LA_{II}) as well as a minor contribution from shallow intra-bandgap states.[23-26, 61] Notably, the EPR spectrum of R600 showed an additional signal centered at g-factor of 1.92. This could originate from e^- migration from intra-bandgap states (*vide supra*) to the empty 3*d*/4*s* sub-shells of $•Ti^{4+}/•Ti^{4+}•$ with phenomenal electrophilicities, resulting in their reduction to $Ti^{3+}/•Ti^{3+}$.[23-26, 61] The emergence of this signal was caused by the strong E_{LAI}/E_{LAII} for R600, which could further be stabilized under low-temperature analytic environments (10 K).[23-26, 61] This proved the centrality of $T_{REDUCTION}$ dialled-in to yield defective TiO_2 with high E_{LAII} or $E_{BA^-H^+}$ suitable to decline $E_{BARRIER}$ for elevation of $^•OH$ productivity via non-optical H_2O_2 homolysis.

Although the catalyst surfaces were potentially featured by the marginality of N_{LAI}/N_{LAII} compared to $N_{BA^-H^+}$ ($N_{LAII}<N_{LAI}<<N_{BA^-H^+}$; hypothesis I), LA_I/LA_{II} profoundly affected the locations and contents of $O_{BRÖNSTED}$ species (BA^- of BA^-H^+) across the surfaces, as proved by their binding energies range (530.8-531.8 eV) and relative contents (6.2-24.7 %; Fig. 3B and Table S4†). Notably, e^- of BA^-H^+ can move toward BA^- more conspicuously and make BA^- less nucleophilic ($E_{BA^-H^+}$↑) particularly at larger N_{LAI}/N_{LAII} or at higher E_{LAI}/E_{LAI} (N_{LAI}/N_{LAII}↑; E_{LAI}/E_{LAII}↑→ $O_{BRÖNSTED}$ binding energy↓). This occurred because neighboring LA_I/LA_{II} could withdraw e^- from BA^-.[19-22, 25] This thereby induced a tentative trend on $E_{BA^-H^+}$ values of O300<R300~R400~R500~R600. However, e^- abundance of BA^- ($E_{BA^-H^+}$) inherent to the surfaces increased in the sequence of O300<R300<R400<R500~R600, as proved by binding energies of their $O_{BRÖNSTED}$ species. This discrepancy could partially be attributed to the congregation of TiO_2 poly-crystallites, which was more pronounced at a higher $T_{REDUCTION}$ and thus dynamically altered the traits of BA^-H^+ sites composing the majority of acidic sites on the surfaces. Nonetheless, hypothesis III ($E_{BA^-H^+}$↑ via H_2 reduction) was proven to permit the prediction that BA^-H^+ sites of R300 (or R600) could outperform those of O300 in facilitating $^•OH$ desorption (RDS) via $E_{BARRIER}$ reduction. Moreover, $O_{BRÖNSTED}$ contents of the surfaces also relied highly on aggregation of TiO_2 particulates, which was more pronounced at a higher $T_{REDUCTION}$. Accordingly, the $O_{BRÖNSTED}$ contents gradually increased in the order of R600~R500<R400<R300<O300. Overall, the XP spectra of the surfaces partially validated the merits of R300 over O300 (hypotheses II-III), as well as those of R600 over R300-R500, in achieving higher E_{LAII} and/or $E_{BA^-H^+}$ proper to prompt the RDS of H_2O_2 homolysis. Nevertheless, in the XP spectral results, the binding energies (e^-/H^+ affinity) of all surface species hinged on N_{LAI}/N_{LAII} that were highly coupled with E_{LAI}/E_{LAII}. In contrast, $O_{CHEMISORBED}$ contents of the surfaces relied primarily on N_{LAI}/N_{LAII}.

Acidic traits of the catalysts: isotherm and TPD

$H_2O_2/^•OH/^•OOH/O_2^{•-}$ possess kinetic diameters (2.4-2.9 Å) similar to those of CO/CO_2 (3.2-3.3 Å).[62, 63] C of CO is coordinate-bonded to LA_{II} (defective $•Ti^{4+}•$ with coordination number of ≤4), whereas C and O of CO_2 are pseudo-hydrogen-bonded to BA^- and H^+ of BA^-H^+, respectively, with O of CO_2 being also coordinate-bonded to LA_{II}.[64-67] Considering hypothesis I ($N_{LAII}<<N_{BA^-H^+}$), CO_2 was expected to bind preferentially with BA^-H^+ rather than with N_{LAII}. Accordingly, CO and CO_2 served as probes for assessing N_{LAII}/E_{LAII} and $N_{BA^-H^+}/E_{BA^-H^+}$ of the catalysts, respectively, as also reported elsewhere.[19, 21, 22] In this regard, the catalysts were subjected to CO or CO_2 isotherm experiments at -10 °C, 0 °C, and 20 °C (near 25 °C), from which the amounts of CO-accessible LA_{II} sites or CO_2-accessible BA^-H^+ sites present in a per-gram of the catalysts ($N_{CO,\ ISO}$ or $N_{CO2,\ ISO}$) as a function of relative pressure (P/P_0) were collected. These isotherms were fitted using the Toth model (Fig. S6-S7†, Table S5-S6†, and Eqn. S3†).[19, 22] The fitted CO or CO_2 isotherms of the catalysts were then implemented to relate the isosteric heats of CO adsorption ($E_{CO,\ ISO}$) with CO coverages ($N_{CO,\ ISO}$) or the isosteric heats of CO_2 adsorption ($E_{CO2,\ ISO}$) with CO_2 coverages ($N_{CO2,\ ISO}$) using the Clausius-Clapeyron equation (Fig. S6F/S7F† and Eqn. S4†).[19, 22] Although the $E_{CO,\ ISO}$ or $E_{CO2,\ ISO}$ values were evaluated near 25 °C, precise quantification of CO binding energies with LA_{II} sites (E_{LAII}) and CO_2 binding energies with BA^-H^+ sites ($E_{BA^-H^+}$) require consideration of the lowest CO and CO_2 coverages, respectively (*i.e.*, minimum $N_{CO,\ ISO}$ and $N_{CO2,\ ISO}$).[19, 22] This is because the increase in $N_{CO,\ ISO}$ (or $N_{CO2,\ ISO}$) brings about either an elevation or reduction of $E_{CO,\ ISO}$ (or $E_{CO2,\ ISO}$). The former arises from multi-layer CO (or CO_2) adsorption on LA_{II} (or BA^-H^+), whereas the latter results from lateral CO-CO (or CO_2-CO_2) interactions above LA_{II} (or BA^-H^+; Fig. S6F/S7F†). There effects can severely distort the $E_{CO,\ ISO}$ and $E_{CO2,\ ISO}$ values of the catalysts and lead frequently to over-estimation of their $N_{LAII}/N_{BA^-H^+}$.[19, 22, 68] Meanwhile, the trend on $E_{CO,\ ISO}$ (~E_{LAII}) values of the catalysts was O300<R300<R400<R500<R600 (Fig. 4C) and matched those on their $O_{LATTICE}$ and $O_{CHEMISORBED}$ electrophilicities. In addition, the trend on $E_{CO2,\ ISO}$ (~$E_{BA^-H^+}$) values of the catalysts was O300<R300<R400~R500<R600 (Fig. 4D), which was in partial

View Article Online
DOI: 10.1039/D6TA01370B

agreement with that on their $O_{BRÖNSTED}$ nucleophilicities (O300<R300<R400<R500~R600). However, these correlations should be interpreted with caution, as the lowest CO and CO_2 coverages used to assess $E_{CO,\ ISO}$ and $E_{CO2,\ ISO}$ values differed markedly ($N_{CO,\ ISO}$ of 0.1-6.7 $\mu mol_{CO}\ g_{CAT}^{-1}$; $N_{CO2,\ ISO}$ of 14.8-83.9 $\mu mol_{CO2}\ g_{CAT}^{-1}$; Fig. S6F/S7F†).[19, 22, 68]

To promote the accuracy of $E_{LAII}/E_{BA^-H^+}$ and $N_{LAII}/N_{BA^-H^+}$ quantification, temperature-programmed desorption (TPD) profiles were collected with the use of CO and CO_2 as probe molecules for LA_{II} and BA^-H^+ sites, respectively.[21, 69-71] Typically, the purged catalysts chemisorbed CO (or CO_2) molecules at 50 °C and heated to 350 °C for desorbing CO (or CO_2) molecules with diverse ramping rates (β) of 3-7 °C min^{-1} (or 2-7 °C min^{-1}).[21, 69-71] The areas under the resulting CO-TPD (or CO_2-TPD) profiles (thermal conductivity detector (TCD) signal *versus* temperature) of the catalysts at distinct β values then served to determine their $N_{CO,\ TPD}$ (~N_{LAII}) (or $N_{CO2,\ TPD}$ (~$N_{BA^-H^+}$)) values, representing the amount of CO-accessible LA_{II} (or CO_2-accessible BA^-H^+) included in a per-gram of the catalyst at 50 °C (near 25 °C; Fig. S8-S9†/S11-S12†).[21, 69-71] In addition, their CO-TPD (or CO_2-TPD) profiles were curve-fitted into three sub-bands (I-III), all of which had peak temperatures (T_{MAX}; Fig. S8-S9†/S11-S12† and Table S7-S8†).[21, 69-71] β and T_{MAX} for the individual sub-bands were thereafter associated by constructing the plots of ln (β/T_{MAX}^2) *versus* $1/T_{MAX}$, whose slopes are identical to ($-E_{CO,\ TPD}/R$) (or ($-E_{CO2,\ TPD}/R$)) values. $E_{CO,\ TPD}$ (or $E_{CO2,\ TPD}$) and R denote the CO (or CO_2) binding energy with LA_{II} (or BA^-H^+) sites innate to the catalysts at 50 °C (near 25 °C) and the ideal gas constant, respectively, according to TPD theory ($E_{CO,\ TPD}$~E_{LAII}; $E_{CO2,\ TPD}$~$E_{BA^-H^+}$; Eqn. S5†), as detailed in Fig. S10/S13† and Table S7-S8†.[21, 69-71]

Interestingly, $N_{CO,\ TPD}$ (~N_{LAII}) values of the catalysts were similar (~50 $nmol_{CO}\ g_{CAT}^{-1}$; Fig. 4A), which indicated that $O_{CHEMISORBED}$ contents used to probe N_{LAI}/N_{LAII} of the catalysts could depend highly on their N_{LAI} values with the hierarchy of R600<R500<R400~R300~O300 (Fig. 3B). Furthermore, $E_{CO,\ TPD}$ values of the catalysts increased in the sequence of O300≤R300≤R400≤R500≤R600, whose hierarchy was in line with those on their $E_{CO,\ ISO}$ values and on their $O_{CHEMISORBED}$ electrophilicities (O300<R300<R400<R500<R600; Fig. 3B/4C). Here, $E_{CO,\ TPD}$ and $E_{CO,\ ISO}$ values of the catalysts reflected their E_{LAII} values, whereas $O_{CHEMISORBED}$ electrophilicities of the catalysts captured the combined contributions of their E_{LAI} and E_{LAII} vales. These rendered it to be compelling that E_{LAI} values of the catalysts increased in the order of O300<R300<R400<R500<R600, thereby validating hypothesis II (E_{LAI}↑ and E_{LAII}↑ via H_2 reduction).

On the other hand, $N_{CO2,\ TPD}$ (~$N_{BA^-H^+}$) values of the catalysts increased in the order of R600<R500<R400~R300~O300, which differed from the trend observed for their $N_{CO,\ TPD}$ values (~N_{LAII}; Fig. 4A-4B). This substantiated that CO_2 could bind primarily with BA^-H^+ sites of the catalysts. Importantly, $N_{CO2,\ TPD}$ (~$N_{BA^-H^+}$) values of the catalysts was ~10^3-fold higher than their $N_{CO,\ TPD}$ values (~N_{LAII}; Fig. 4A-4B), which corroborated hypothesis I that BA^-H^+ and LA_I/LA_{II} constituted the majority and minority of acidic sites innate to the catalysts, respectively ($N_{LAII}<N_{LAI}<<N_{BA^-H^+}$ via O_2 calcination/H_2 reduction). Moreover, $E_{CO2,\ TPD}$ (~$E_{BA^-H^+}$) values of the catalysts were elevated in the sequence of O300≤R300≤R400≤R500<R600 (Fig. 4D), thereby proving hypothesis III ($E_{BA^-H^+}$↑ via H_2 reduction). Notably, $E_{CO2,\ TPD}$ (~$E_{BA^-H^+}$) values of the individual catalysts were 10-15 kJ mol^{-1} lower than their corresponding $E_{CO,\ TPD}$ (~E_{LAII}) values except for R600 (~68.8 kJ mol_{CO}^{-1} for $E_{CO,\ TPD}$; ~66.4 kJ mol_{CO2}^{-1} for $E_{CO2\text{-}TPD}$; Fig. 4C-4D), thereby demonstrating hypothesis IV ($E_{BA^-H^+}<E_{LAII}$). This indicated the energy needed to detach the H atom of •OH from BA^- of BA^-H^+ was higher than that required to withdraw the O atom of •OH from LA_{II} throughout the catalyst surfaces. This substantiated hypotheses V-VI that BA^-H^+ could function as the major activator of H_2O_2 homolysis and thereby outweighed LA_{II} in dictating the RDS (•OH desorption from BA^-H^+; Fig. 1D) in conjunction with the demonstration of preferential H_2O_2 adsorption on BA^-H^+ over LA_{II} .

NH_3 can readily coordinate with BA^-H^+ and LA_{II} to form $BA^-NH_4^+$ and LA-NH_3, respectively, on the catalyst surface with their NH_3 binding strengths being lower at higher surface temperatures.[21, 37] NH_3 was thus utilized as a probe molecule to further evaluate the acidic features of O300/R300/R600 via *in situ* NH_3-diffuse reflectance infrared Fourier transform (DRIFT) spectroscopy technique. The choice of O300/R300/R600 for these experiments originated from their distinct $N_{BA^-H^+}/N_{LAII}$ and $E_{BA^-H^+}/E_{LAII}$ characteristics.[21, 37] Typically, the purged catalysts were exposed sequentially to a N_2 and NH_3/N_2 for recording their background signals and their *in situ* NH_3 spectral signals, respectively, at 50 °C or at 150 °C (Fig. S14†).[21, 37] The resulting background-corrected, *in situ* NH_3-DRIFT spectra of the catalysts revealed multiple bands, resulting from asymmetric (ASYM)/symmetric (SYM) stretching (STR)/wagging vibrations of O-H bonds inherent to $BA^-NH_4^+$ species or N-H bonds innate to $BA^-NH_4^+/LA_{II}$-NH_3 species.[21, 37] Notably, bands centered at wavenumbers of <3,000 cm^{-1} were unsuitable for quantitative comparison of acidic traits for the catalysts due to significant band overlaps and baseline distortion.[21, 37] Conversely, bands centered at wavenumbers of ≥3,000 cm^{-1} were well-resolved, thus allowing for comparison of $N_{BA^-H^+}$ and N_{LAII} values for the catalysts using the areas under bands indexed to $BA^-H^+_{ASYM/STR}$ and $LA_{II\ ASYM/STR}/LA_{II\ SYM/STR}$, respectively.[21, 37] The areas under $LA_{II\ ASYM/STR}/LA_{II\ SYM/STR}$ bands were nearly identical across all the catalysts at 50 °C or at 150 °C, supporting the comparable $N_{CO,\ TPD}$ (N_{LAII}) values for O300~R300~R600. In contrast, the area under $BA^-H^+_{ASYM}$ band was higher in the sequence of R600<R300~O300 at 50 °C or at 150 °C, which was in accordance with their $N_{CO2,\ TPD}$ ($N_{BA^-H^+}$) hierarchy. Again, the elevation of analytic (surface) temperature from 50 °C to 150 °C led to a decrease in band areas with the extent of band area reduction being more pronounced at a lower E_{LAII} or a lower $E_{BA^-H^+}$.[21, 37] Apparently, areas under the $LA_{II\ ASYM/STR}/LA_{II\ SYM/STR}$ bands of the catalysts were comparable and revealed minimal dependence of analytic temperatures, further verifying $E_{CO,\ TPD}$ (E_{LAII}) values of O300~R300~R600. Meanwhile, areas under the $BA^-H^+_{ASYM/STR}$ bands for O300 and R300 decreased substantially with their surfaces being heated. This was opposed to the trend on areas under the $BA^-H^+_{ASYM/STR}$ bands for R600 with surface temperature elevation from 50 °C to 150 °C, substantiating $E_{CO2,\ TPD}$ ($E_{BA^-H^+}$) hierarchy of O300≤R300<R600.

View Article Online
DOI: 10.1039/D6TA01370B

Catalytic H_2O_2 homolysis: rate law

H_2O_2 homolysis efficiencies ($^{\bullet}$OH productivities) of the catalysts in a per-gram basis can rely on their $N_{BA^-H^+}$, $E_{BA^-H^+}$, N_{LAII}, and E_{LAII} (Fig. 1D).[19-22] Therefore, for rigorous comparison, these should be assessed in a per-major active site (BA^-H^+) basis, considering both the energetic burdens ($E_{BARRIER}$) and the frequencies of H_2O_2 collisions with BA^-H^+ and/or LA_{II} sites in a per-unit time (k_{APP}'). Both $E_{BARRIER}$ and k_{APP}' of the catalysts were found to hinge on their BA^-H^+ properties, as evidenced by the derivation of rate law for H_2O_2 homolysis ($-r_{H2O2,\,0,\,CO2}$; *vide infra*) alongside with the relationships of $E_{BA^-H^+}<E_{LAII}$ (associated with $E_{BARRIER}$) and $N_{LAII}<<N_{BA^-H^+}$ (associated with k_{APP}').

Again, H_2O_2 homolysis proceeds through five elementary steps (Fig. 1D): H_2O_2 adsorption via its linkages (hydrogen bonds) with two BA^-H^+ (BA^-: S_1) to generate $2S_1{\bullet}H_2O_2$ (Eqn. 1), $2S_1{\bullet}H_2O_2$ distortion via its coordination with a LA_{II} (S_2) to yield $2S_1{\bullet}H_2O_2{\bullet}S_2$ (Eqn. 2), $2S_1{\bullet}H_2O_2{\bullet}S_2$ dissection via its coordination with an additional S_2 to form two $S_1{\bullet}{}^{\bullet}OH{\bullet}S_2$ (Eqn. 3), disintegration of two $S_1{\bullet}{}^{\bullet}OH{\bullet}S_2$ species via S_2 detachment to produce two $S_1{\bullet}{}^{\bullet}OH$ (Eqn. 4), and disintegration of two $S_1{\bullet}{}^{\bullet}OH$ species via S_1 detachment to release two $^{\bullet}OH$ to the aqueous phase (Eqn. 5), as summarized in Table S9†.[19-22]

$$2S_1 + H_2O_2 \overset{K_1}{\leftrightarrow} 2S_1 \cdot H_2O_2 \text{ (1)}$$

$$2S_1 \cdot H_2O_2 + S_2 \overset{K_2}{\leftrightarrow} 2S_1 \cdot H_2O_2 \cdot S_2 \text{ (2)}$$

$$2S_1 \cdot H_2O_2 \cdot S_2 + S_2 \overset{K_3}{\leftrightarrow} 2(S_1 \cdot {}^{\bullet}OH \cdot S_2) \text{ (3)}$$

$$2(S_1 \cdot {}^{\bullet}OH \cdot S_2) \overset{K_4}{\leftrightarrow} 2(S_1 \cdot {}^{\bullet}OH) + 2S_2 \text{ (4)}$$

$$2(S_1 \cdot {}^{\bullet}OH) \overset{k_5}{\rightarrow} 2S_1 + 2{}^{\bullet}OH \text{ (5)}$$

Eqn. 5 is more endoergic than Eqn. 4 ($E_{BA^-H^+}<E_{LAII}$) and thereby could be considered as the RDS of H_2O_2 homolysis, in which K_1-K_4, k_5, C_i, and [j] indicate the quasi-equilibrium constants for Eqn. 1-4 at or near standard states (25 °C and 1 atm), the forward reaction rate constant for Eqn. 5, the concentration of aqueous species i, and the concentration of surface species j, respectively. Site balances were thereafter formulated for S_1 and S_2 (Eqn. 6 and Table S9†), where the content of S_1 could be substantially higher than that of S_2 ([S_2]<<[S_1]), as boosted by their initial quantities of $N_{LAII}<<N_{BA^-H^+}$ in 100 mL of aqueous reaction medium ([S_2]$_0$<<[S_1]$_0$). Accordingly, the terms of [S_1]$_0$-[S_2]$_0$ and [S_1]-[S_2] could be simplified into [S_1]$_0$ and [S_1], respectively, as depicted in Eqn. 7.

$$[S_1]_0 - [S_2]_0 = [S_1] - [S_2] + [S_1]\left(K_1 C_{H2O2}[S_1] + K_1^{0.5}K_2^{0.5}K_3^{0.5}K_4^{0.5}C_{H2O2}^{0.5}\right) \text{ (6)}$$

$$[S_1]_0 = [S_1]\left(1 + K_1 C_{H2O2}[S_1] + K_1^{0.5}K_2^{0.5}K_3^{0.5}K_4^{0.5}C_{H2O2}^{0.5}\right) \sim [S_1] \text{ (7)}$$

Moreover, the equilibrium constant of H_2O_2 adsorption on S_2 sites of Au/titanium silicate or Fe/silicon carbide (S_2+H_2O_2↔$S_2{\bullet}H_2O_2$) was reported to be ≤~10^1 L mol^{-1} under near standard conditions.[72, 73] Hence, K_1 could be reasonably estimated as ≤~10^1 L^2 mol^{-2}, considering that E_{LAII} values ($E_{CO,\,TPD}$ of 45-70 kJ mol$_{CO}^{-1}$; Fig. 4C) of the catalysts were in similar magnitude with their $E_{BA^-H^+}$ counterparts ($E_{CO2,\,TPD}$ of 35-70 kJ mol$_{CO2}^{-1}$; Fig. 4D), albeit with the hierarchies of $E_{BA^-H^+}<E_{LAII}$ for the individual catalysts. In addition, $S_2<<S_1$ of the catalysts suggested that S_2 sites vicinal to two S_1 sites could be rare, thus making the endothermic quasi-equilibria for H_2O_2 distortion (Eqn. 2) and $^{\bullet}OH$ desorption from S_2 (Eqn. 4) be shifted to the left, while K_2 and K_4 values could be lower than K_1. A similar constraint applied to the exoergic quasi-equilibrium of H_2O_2 dissection (Eqn. 3), whose K_3 could thus be only slightly higher than 10^0 and below 10^1. Overall, it was logically sound to approximate K_1, K_2, K_3, and K_4 as ≤~10^1 L^2 mol^{-2}, <~10^0 L mol^{-1}, ~10^0, and <~10^0 mol^2 L^{-2}, respectively.

Meanwhile, the H_2O_2 concentrations (C_{H2O2}) evolved upon exposure of the catalysts to reaction (aqueous electric) conditions were evaluated to be ≤~5.4X10^{-3} mol$_{H2O2}$ L^{-1} (Fig. S17†; *vide infra*). Furthermore, [S_1] values of the catalysts should be similar to or smaller than their [S_1]$_0$ counterparts. Here, [S_1]$_0$ values corresponded to the moles of BA^- (or BA^-H^+) present in 0.2g of the catalysts soaked in 100 mL of aqueous reaction media ($C_{BA^-H^+,\,0.2g}$~$C_{CO2\text{-}TPD,\,0.2\,g}$) and were assessed to be ≤~3.6X10^{-4} mol$_{BA^-H^+}$ L^{-1}, as detailed in Table S9†. All of these were gathered to render the terms of $K_1C_{H2O2}[S_1]$ and $K_1^{0.5}K_2^{0.5}K_3^{0.5}K_4^{0.5}C_{H2O2}^{0.5}$ located on the left-hand side of Eqn. 7 to be <<1, permitting to simplify Eqn. 7 into [S_1]$_0$~[S_1].

The H_2O_2 dissection rate ($-r_{H2O2}$) is defined by the moles of H_2O_2 dissected in a per-unit volume and in a per-unit time (Eqn. 8). $-r_{H2O2}$ served to represent initial H_2O_2 dissection rate ($-r_{H2O2,\,0,\,CO2}$) defined by the moles of H_2O_2 initially dissected in a per-CO_2-accessible BA^-H^+ and in a per-unit time upon the reformulation of Eqn. 8 using $C_{CO2\text{-}TPD,\,0.2\,g}$ (~[S_1]$_0$) along with the substitution of the initial aqueous H_2O_2 concentration ($C_{H2O2,\,0}$) and [S_1]$_0$ for C_{H2O2} and [S_1], respectively (Eqn. 9 and Table S9†).[19-22]

$$-r_{H2O2} = k_5K_1K_2K_3K_4C_{H2O2}[S_1]^2 \text{ (8)}$$

$$-r_{H2O2,\,0,CO2} = \frac{\left(k_5K_1K_2K_3K_4[S_1]_0^2\right)C_{H2O2,\,0}}{C_{CO2,\,TPD,\,0.2g}} = \left(k_5K_1K_2K_3K_4[S_1]_0\right)C_{H2O2,\,0} \text{ (9)}$$

Notably, $-r_{H2O2,\,0,\,CO2}$ values of the catalysts remained formidable to directly evaluate owing to the self-dissection of H_2O_2 to $^{\bullet}OH$/$^{\bullet}OOH$/$O_2^{\bullet-}$ even in the absence of the catalysts under aqueous electric phases, in addition to the difficulty in precisely tracing $^{\bullet}OH$/$^{\bullet}OOH$/$O_2^{\bullet-}$ contents with short lifetimes of ≤~10^7 μseconds.[19-22, 74, 75] Therefore, $-r_{H2O2,\,0,\,CO2}$ values of the catalysts were assessed indirectly using acetaminophen as a model of aqueous wastes. Acetaminophen is particularly suitable because it preferentially undergoes fragmentation via $^{\bullet}OH$-enabled addition or H$^{\bullet}$ abstraction compared with the other organics being examined herein (Fig. 11A).[76-78] This was primarily because the energy needed to take e$^-$ away from e$^-$-donating group (-OH/-NH/-NH$_2$) is lower in acetaminophen than in the other organics (Table S19†), whereas the other organics were more prone to disintegration via (H^+-couple) e$^-$ transfer on $SO_4^{\bullet-}$, $NO_3^{\bullet}$, $H_2PO_4^{\bullet}$, or Fe^{IV}=O, as we investigated earlier.[21, 37, 62, 76-79] Moreover, acetaminophen subjected to $^{\bullet}OH$ addition or H$^{\bullet}$ abstraction readily yields oligomers containing -OH/-NH/-NH$_2$ groups, all of which can strongly interact with and poison $^{\bullet}OH$ generators (BA^-H^+/LA_{II}).[80, 81] Consequently, acetaminophen degradation efficiencies on the catalysts could be deemed as a useful probe to compare their activities, resistances to oligomer formation, and reusabilities in $^{\bullet}OH$ production via H_2O_2 homolysis, if $^{\bullet}OH$ acted as the dominant degrader of acetaminophen and if diffusional constraint between H_2O_2 and BA^-H+/LA_{II} or between $^{\bullet}OH$ and acetaminophen were

View Article Online
DOI: 10.1039/D0TA01339B

negligible. In this context, the initial acetaminophen degradation rate ($-r_{ACETAMINOPHEN,\ 0,\ CO2}$) defined by the moles of acetaminophen initially decomposed in a per-CO_2-accessible BA^--H^+ and in a per-unit time could be represented using a pseudo-1st-order kinetic model (Eqn. 10/S7†).[19-22] Moreover, $-r_{ACETAMINOPHEN,\ 0,\ CO2}$ could be identical to $-r_{H2O2,\ 0,\ CO2}$, where k_{APP} and $C_{ACETAMINOPHEN,\ 0}$ denote the lumped apparent reaction rate constant and the initial aqueous acetaminophen concentration, respectively (Table S9†).[19-22]

$$-r_{ACETAMINOPHEN,\ 0,\ CO2} = \frac{k_{APP} C_{ACETAMINOPHEN,\ 0}}{C_{CO2,\ TPD,\ 0.2g}} = \underbrace{\frac{(k_5 K_1 K_2 K_3 K_4 [S_1]_0) C_{H2O2,\ 0}}{C_{ACETAMINOPHEN,\ 0}}}_{\frac{k_{APP}}{C_{CO2,\ TPD,\ 0.2g}}} \times C_{ACETAMINOPHEN,\ 0} \quad (10)$$

Notably, the RDS of H_2O_2 homolysis (Eqn. 5) was expected to obey Arrhenius behavior, from which k_5 could be represented using the Arrhenius equation (Eqn. 11). k_5', k_{APP}', and $T_{REACTION}$ are referred to as the pre-factor of the RDS, the lumped pre-factor, and the reaction temperature, respectively (Table S9†).[19-22]

$$-r_{ACETAMINOPHEN,\ 0,\ CO2} = \underbrace{\frac{k_5' K_1 K_2 K_3 K_4 [S_1]_0 C_{H2O2,\ 0}}{C_{ACETAMINOPHEN,\ 0}}}_{\frac{k_{APP}}{C_{CO2,\ TPD,\ 0.2g}}} \times C_{ACETAMINOPHEN,\ 0} \times e^{\frac{-E_{BARRIER}}{R \times T_{REACTION}}} \quad (11)$$

Obviously, k_{APP}' (Eqn. 12) and $E_{BARRIER}$ (Eqn. 11) were found to rely highly on $[S_1]_0$ ($\sim C_{CO2,\ TPD,\ 0.2\ g} \sim C_{BA^-H+,\ 0.2g}$) and E_{BA^-H+}, respectively, indicating that BA^--H^+ sites could play a more dominant role than LA_{II} counterparts in directing $-r_{ACETAMINOPHEN,\ 0,\ CO2}$ ($\sim -r_{H2O2,\ 0,\ CO2}$).

$$k_{APP}' = \frac{k_5' K_1 K_2 K_3 K_4 [S_1]_0^2 C_{H2O2,\ 0}}{C_{ACETAMINOPHEN,\ 0}} \quad (12)$$

In addition, to make the claims on $-r_{ACETAMINOPHEN,\ 0,\ CO2} \sim -r_{H2O2,\ 0,\ CO2}$ and on Arrhenius relationships (Eqn. 10-12) valid, $E_{BARRIER}$ values associated with all •OH-mediated acetaminophen degradation routes had to be insignificant. This has previously been demonstrated by a spectrum of computational studies on •OH-induced decomposition of aqueous organics.[82, 83] Furthermore, the equivalence of $-r_{ACETAMINOPHEN,\ 0,\ CO2} \sim -r_{H2O2,\ 0,\ CO2}$ could be compelling if the catalyst scarcely leached one of H_2O_2 evolvers (LA_{II}) to the aqueous phase under electric conditions, which could be verified by filtration runs (*vide infra*). Again, $-r_{ACETAMINOPHEN,\ 0,\ CO2} \sim -r_{H2O2,\ 0,\ CO2}$ could also be contingent upon negligible mass-transfer limitations for both H_2O_2 transport to BA^--H^+/LA_{II} sites and •OH transport to acetaminophen, as demonstrated by diffusion runs (*vide infra*). Finally, $•OOH/O_2^{•-}$ should be marginal relative to •OH in acetaminophen disintegration, as substantiated by scavenging runs (*vide infra*).

Catalytic H_2O_2 homolysis: kinetic assessment

For kinetic inspection of H_2O_2 homolysis upon validation of $-r_{H2O2,\ 0,\ CO2} \sim -r_{ACETAMINOPHEN,\ 0,\ CO2}$, O300, R300, and R600 were selected owing to their distinct Brönsted acidities including O300≤R300<R600 for E_{BA^-H+} and R600<R300~O300 for N_{BA^-H+}. These trends suggested that R600 should unveil the lowest $E_{BARRIER}$ ($-r_{H2O2,\ 0,\ CO2}$ (or $-r_{ACETAMINOPHEN,\ 0,\ CO2}$)↑; Eqn. 11) and the lowest k_{APP}' ($-r_{H2O2,\ 0,\ CO2}$ (or $-r_{ACETAMINOPHEN,\ 0,\ CO2}$)↓; Eqn. 12), where these opposing effects were anticipated to compete in determining $-r_{H2O2}$ (or $-r_{ACETAMINOPHEN,\ 0,\ CO2}$) for R600.

Acetaminophen was degraded under aqueous electric conditions. A bare graphite plate (anode) and a catalyst (0.2 g)-coated graphite plate (cathode) were immersed in 100 mL of an aqueous acetaminophen solution ($1.0X10^{-3}$ mol L^{-1}) containing Na_2SO_4 as the supporting electrolyte with an electric input being applied.[19-21, 79] At the anode, H_2O can be oxidized via $H_2O \rightarrow 2H^+ + 1/2O_2 + 2e^-$. The generated H^+, O_2, and e^- then migrate to the cathode, where H_2O_2 is continuously generated via $2H^+ + O_2 + 2e^- \rightarrow H_2O_2$ as long as an electric input is maintained across the electrodes.[19-21, 79] An electric potential of 3 V was selected to maximize C_{H2O2} values at or near the catalyst surfaces, while minimizing the release of the catalysts from the cathode to the aqueous phase.[19-21, 79] Moreover, H_2O oxidation at the anode can also proceed via $H_2O \rightarrow H^+ + •OH + e^-$, where •OH can react with the anode surface to form surface O highly prone to degrade acetaminophen (anodic oxidation).[19-21, 79] Moreover, H_2O_2 produced at or near the cathode tends to undergo self-cleavage to generate •OH, •OOH, or $O_2^{•-}$, all of which can also participate in acetaminophen degradation (H_2O_2 self-dissection).[19-21, 79] Anodic oxidation and H_2O_2 self-dissection were regarded as backgrounds and thereby served to correct kinetic datasets of acetaminophen conversion ($X_{ACETAMINOPHEN}$; Eqn. S6†) as a function of time. $X_{ACETAMINOPHEN}$ values of <25 % were selected to shift the equilibrium of acetaminophen degradation (or H_2O_2 homolysis) to the right at $T_{REACTION}$ values of 25-55 °C.[19-21, 79] The kinetic datasets subjected to background correction were then fitted using a pseudo-1st-order kinetic model to evaluate k_{APP} values (Fig. S16/S18/S20-S21/S24/S27† and Table S10†), with which background-corrected $-r_{ACETAMINOPHEN,\ 0,\ CO2}$ and initial acetaminophen degradation rate defined by the moles of acetaminophen initially decomposed in a per-gram and in a per-unit time ($-r_{ACETAMINOPHEN,\ 0}$; Eqn. S8†) were assessed.[19-21, 79] Importantly, $-r_{ACETAMINOPHEN,\ 0,\ CO2}$ and $-r_{ACETAMINOPHEN,\ 0}$ of the catalysts served to compare their activities and recyclabilities in decomposing acetaminophen, respectively, whereas $-r_{POLLUTANT,\ 0,\ CO2}$ values were also used to compare the adaptabilities of the catalysts in disintegration of other aqueous organic pollutants.[19-21, 79]

Notably, acetaminophen degradation should proceed under LA_{II} leaching-free aqueous electric environments, under which the presumption concerning the rarity of S_2 (LA_{II}) sites vicinal to two S_1 (BA^-) sites for use in deriving $-r_{H2O2,\ 0,\ CO2}$ (Eqn. 9) and $-r_{ACETAMINOPHEN,\ 0,\ CO2}$ (Eqn. 11) could remain valid. To verify this, acetaminophen degradation runs were performed at 3 V and 25 °C up to 360 minutes according to the methods depicted earlier and in the caption of Fig. S15†.[19-21, 79] Exceptions were the replacement of the catalyst-coated cathodes with bare graphite electrodes at 60 minutes, where the aqueous reaction solutions were filtered to collect the corresponding reaction filtrates (Fig. S15B-S15D†).[19-21, 79] Acetaminophen degradation runs were then resumed using two bare graphite plates soaked in the aqueous reaction filtrates for monitoring $X_{ACETAMINOPHEN}$ values at 60-360 minutes (filtration runs). $X_{ACETAMINOPHEN}$ values monitored in the filtration runs could originate from anodic oxidation, $•OH/•OOH/O_2^{•-}$ generated via H_2O_2 self-dissection,

View Article Online
DOI: 10.1039/D6TA01330B

and those produced via homogeneous H_2O_2 homolysis on leached LA_{II} and aqueous OH^- (BA^--H^+).[19-21, 79] For comparison, acetaminophen degradation control run was conducted using two bare graphite electrodes at 3 V and 25 °C up to 360 minutes, where $X_{ACETAMINOPHEN}$ values could arise only from anodic oxidation and $^{\bullet}OH/^{\bullet}OOH/O_2^{\bullet-}$ generated via H_2O_2 self-dissection (blank run; Fig. S15A†).[19-21, 79] The extent of acetaminophen degradation between 60 and 360 minutes ($\Delta C_{ACETAMINOPHEN}$ or the change in $X_{ACETAMINOPHEN}$ values) was similar for the filtration and blank runs (~$0.4X10^{-3}$ $mol_{ACETAMINOPHEN}$ mol^{-1}). This indicated that H_2O_2 homolysis contributed negligibly to $^{\bullet}OH/^{\bullet}OOH/O_2^{\bullet-}$ production, confirming that LA_{II} quantities leached from the catalyst surfaces were minimal under the aqueous electric phases.

Acetaminophen decomposition should proceed under reaction-controlled environments without significant internal or external mass-transfer limitations. In particular, diffusion of H_2O_2 to BA^--H^+/LA_{II} sites and that of $^{\bullet}OH$ to acetaminophen should not dominate the observed kinetics under aqueous electric conditions. In this context, acetaminophen degradation runs were performed at 3 V and 25 °C for 6 minutes, while varying catalyst particulate size (<90 μm, 90-200 μm, and <200 μm) or stirring speed (300 rpm and 400 rpm) with the former and the latter being utilized to inspect the repercussions of internal and external diffusions on $-r_{ACETAMINOPHEN, 0, CO2}$ values of the catalysts, respectively (diffusion runs; Fig. S16† and Table S10†).[19-21, 79] The resulting $-r_{ACETAMINOPHEN, 0, CO2}$ values of the catalysts were essentially independent of both particulate size or stirring speed (Fig. 5A). This indicated that $-r_{ACETAMINOPHEN, 0, CO2}$ values were evaluated in reaction-limited domains and were barely affected by mass-transfer limitations of H_2O_2 transport to BA^--H^+/LA_{II} sites or $^{\bullet}OH$ transport to acetaminophen. Accordingly, acetaminophen (or aqueous contaminant) degradation runs were conducted using 0.2 g of the catalyst with sizes of <200 μm at an electric input of 3 V, a $T_{REACTION}$ of 25 °C, and a stirring speed of 300 rpm, unless otherwise specified. Inductively coupled plasma-atomic emission spectroscopy (ICP-AES) served to quantify Ti leaching during the diffusion runs. All the catalysts released minute Ti contents (<10^{-4} mol. %) to aqueous phases, which was in line with the results on the filtration runs (Fig. S15†). These could be gathered with the results on the diffusion runs (Fig. 5A) to support the validity of $-r_{H2O2, 0, CO2}$~$-r_{ACETAMINOPHEN, 0, CO2}$ for the catalysts. Importantly, $-r_{ACETAMINOPHEN, 0, CO2}$ values of O300 and R300 were comparable (~0.02 min^{-1}), yet, were only around a fifth of that for R600. This suggested that $E_{BARRIER}$ could outstrip k_{APP}' in determining $-r_{ACETAMINOPHEN, 0, CO2}$ of R600, highlighting the merit of H_2 reduction-subjected, defective TiO_2 (R600) for $^{\bullet}OH$ generation via non-optical H_2O_2 activation.

Notably, acetaminophen degradation should primarily be driven by $^{\bullet}OH$ rather than $^{\bullet}OOH/O_2^{\bullet-}$ under aqueous electric environments. At circum-neutral pH values (4.5-7.0), $^{\bullet}OOH$ readily deprotonates to form $O_2^{\bullet-}$, thus making it challenging to conclude which reactive oxygen species (ROS; $^{\bullet}OH$, $^{\bullet}OOH$, or $O_2^{\bullet-}$) could dominate acetaminophen degradation.[21, 34] H_2O_2 evolution runs were thus carried out identically to the diffusion runs except for the exclusion of acetaminophen from aqueous reaction solutions with C_{H2O2} values being monitored up to 30 minutes (Fig. S17†).[19-21, 79] The C_{H2O2} values rapidly increased and plateaued within 5-30 minutes with averaged C_{H2O2} ($C_{H2O2, AVG}$) values in the range of $2.6X10^{-3}$-$5.4X10^{-3}$ mol_{H2O2} L^{-1}. The observed trend on $C_{H2O2, AVG}$ values did not correlate with the acidic traits of the catalysts, yet, fell outside the scope of the current study and therefore was not further elaborated.

Instead, the C_{H2O2} values monitored at ≥5 minutes were averaged and doubled to determine the scavenger content added to the aqueous reaction solution ($8.2X10^{-3}$ $mol_{SCAVENGER}$ L^{-1}). The quenching rate of $^{\bullet}OH$, $^{\bullet}OOH$, or $O_2^{\bullet-}$ can depend highly on the type of the scavenger utilized, as corroborated by its 2nd-order rate constants for ROS removal (k_{ROS}↑→$-r_{ACETAMINOPHEN, 0, CO2}$↓; Table S11†).[84-86] To this end, acetaminophen degradation runs were performed identically to the diffusion runs except for the inclusion of a scavenger (catechol or hydroquinone) in aqueous reaction solutions (scavenging runs; Fig. S18† and Table S10†). The pH range was comparable to that of the diffusion runs (4.5-7.0),[19-21, 79] suggesting that $^{\bullet}OH/^{\bullet}OOH/O_2^{\bullet-}$ generation was of likelihood across the scavenging runs. The $-r_{ACETAMINOPHEN, 0, CO2}$ values of the individual catalysts increased in the sequence of 'with catechol'~'with hydroquinone'<'without scavenger' (Fig. 5B). This trend was inconsistent with those on $-r_{ACETAMINOPHEN, 0, CO2}$ values anticipated with the speculation that either $^{\bullet}OOH$ or $O_2^{\bullet-}$ could function as the main degrader of acetaminophen ('with hydroquinone'<'with catechol'<'without scavenger'). The hierarchy on $-r_{ACETAMINOPHEN, 0, CO2}$ values of the individual catalysts, however, was in agreement with that expected with the assumption that $^{\bullet}OH$ could act as the major decomposer of acetaminophen, thereby boosting the claim that $^{\bullet}OH$ outcompeted $^{\bullet}OOH/O_2^{\bullet-}$ in acetaminophen disintegration in addition to demonstration of $-r_{H2O2, 0, CO2}$~$-r_{ACETAMINOPHEN, 0, CO2}$.

Catalytic H_2O_2 homolysis: EPR spectroscopy and kinetic parameter

$^{\bullet}OH$ bound to LA_{II}/BA^--H^+ sites can react with aqueous H_2O_2 to form $^{\bullet}OOH$ species bound to these sites (poison I). At pH values of ≥4.8, some of these $^{\bullet}OOH$ species undergo deprotonation to yield $O_2^{\bullet-}$ species bound to LA_{II} sites (poison II; Fig. 8A).[21, 34] The $^{\bullet}OOH/O_2^{\bullet-}$ species can poison H_2O_2 activators (LA_{II}/BA^--H^+), unless these are released to the aqueous media via desorption from LA_{II}/BA^--H^+ sites.[21, 34] Aqueous $^{\bullet}OH$ productivities increased in the sequence of O300~R300<R600, as evidenced by the hierarchy on their $-r_{ACETAMINOPHEN, 0, CO2}$ (~$-r_{H2O2, 0, CO2}$) values assessed from the diffusion runs. In contrast, aqueous $^{\bullet}OOH$ productivities were expected to be lower for R600 than for R300 (or O300). This was ascribed to higher E_{LAII} and E_{BA-H+} values of R600, whose surface could desorb $^{\bullet}OH$ species from LA_{II}/BA^--H^+ sites more promptly than the others. As a result, $^{\bullet}OH$ species bound to R600 surface has a lower probability to react with H_2O_2 for yielding $^{\bullet}OOH$ species (poison I). Similarly, aqueous $O_2^{\bullet-}$ productivities were also predicted to be lower for R600 than for R300 (or O300), considering their hypothetic coverages of $^{\bullet}OOH$ species functioning as $O_2^{\bullet-}$ precursors (R600<R300~O300) coupled with the comparable pH range (4.5-7.0) across all catalysts immersed in aqueous electric conditions (*i.e.*, similar tendencies of $^{\bullet}OOH$→$O_2^{\bullet-}$).

View Article Online DOI: 10.1039/D6TA01739B

Overall, aqueous •OH and •OOH/$O_2^{•-}$ productivities were expected to increase in the sequence of O300~R300<R600 and R600<R300~O300, respectively (*vide supra*). These hypotheses were investigated via EPR spectroscopy experiments.[19-22] The catalysts were mixed with aqueous H_2O_2 to form aqueous reaction mixtures, where the quantity of H_2O_2 was regulated to be in excess relative to that of BA^--H^+ sites for the catalyst, given $C_{BA^-H^+,\ 0.2g} << C_{H2O2}$ in the diffusion runs (Fig. S17†).[19-22] Notably, 5,5-dimethyl-1-pyrroline N-oxide (DMPO) can be adducted to aqueous •OH and aqueous •OOH/$O_2^{•-}$ for trapping their spins via production of aqueous DMPO-OH and aqueous DMPO-OOH, respectively (* and **; Fig. 6A).[19-22] Moreover, a fraction of aqueous DMPO-OH adducts can transform into aqueous HDMPO analogues via adsorption on LA_{II} sites (defective Ti^{4+}; ****; Fig. 6B) followed by deprotonation (***; Fig. 6B) and desorption from •LA_{II} sites (defective •Ti^{4+}; *****; Fig. 6B).[19-22] Notably, the adsorption stage marked with **** could be decelerated on the catalyst surface with a higher E_{LAII}, whereas the deprotonation stage marked with *** could proceed similarly across all the catalyst surfaces due to similar pH range of the corresponding aqueous reaction solutions subjected to EPR spectroscopy experiments (*vide infra*). All of these were coupled with the trend on N_{LAII} values of O300~R300~R600 to induce the speculation that aqueous HDMPO productivities could increase in the order of R600<O300~R300. Furthermore, aqueous HDMPO can also be adducted to aqueous •OH to yield aqueous HDMPO-OH, which made it convincing that aqueous HDMPO-OH contents should be included in the quantification of aqueous •OH productivities on the catalyst surfaces.[19-22]

To this end, the aqueous reaction mixtures stated above were then mixed with DMPO, stirred vigorously, and filtered to isolate aqueous reaction solutions with pH values of 4.2, under which a fraction of •OOH poisons could transform into $O_2^{•-}$ counterparts on the catalyst surfaces exposed to aqueous H_2O_2 conditions.[19-22] The aqueous reaction solutions were subjected to EPR spectroscopy experiments at 25 °C. The resulting EPR spectra were curve-fitted according to the methods outlined in Table S12† for identifying DMPO adducts and quantifying their concentrations (Fig. 6C-6E and Table S13†).[19-22] The EPR spectra disclosed three characteristic signal patterns: a quartet-signal set with an intensity ratio of 1:2:2:1 assigned to aqueous DMPO-OH, a sextet-signal set with an intensity ratio of 1:1:1:1:1:1 indexed to aqueous DMPO-OOH, and a trio-signal set with an intensity ratio of 1:1:1 assigned to aqueous HDMPO-OH.[19, 22, 87-90] The aqueous HDMPO-OH contents increased in the order of R600 (5.6 %)<R300~O300 (16.7-20.8 %), which was in accordance with the trend anticipated (R600<R300~O300). Moreover, the combined contents of the aqueous DMPO-OH and aqueous HDMPO-OH increased in the sequence of O300 (66.7 %)<R300~R600 (83.3-88.9 %), which was in partial line with aqueous •OH productivities inferred from $-r_{ACETAMINOPHEN,\ 0,\ CO2}$ values (O300~R300<R600) and supported the conclusion that defective TiO_2 subjected to H_2 reduction at 600 °C could maximize acceleration of H_2O_2 homolysis under aqueous phases. Conversely, the aqueous DMPO-OOH contents increased in the order of R600~R300 (11.1-16.7 %)<O300 (33.3 %), which partially matched our prediction depicted earlier (R600<R300~O300). This suggested that H_2 reduction-subjected, defective TiO_2 could reveal greater tolerance to •OOH/$O_2^{•-}$ poisons than H_2 reduction-unsubjected TiO_2 (O300), thereby tentatively sustaining H_2O_2 homolysis more effectively under aqueous conditions. Importantly, aqueous •OH-induced DMPO adducts of aqueous DMPO-OH and HDMPO-OH accounted for the majority of aqueous DMPO adducts monitored earlier (66.7-88.9 %). This could further substantiate that aqueous •OH was the primary reactive species responsible for acetaminophen degradation.

Notably, aqueous DMPO-OOH might be decomposed to form aqueous DMPO-OH, which should be considered for rigor of our quantitative elaboration of all aqueous DMPO adducts.[91, 92] To this end, ethanol (CH_3CH_2OH) served as a •OH quencher due to its high $k_{•OH}$ of $1.9X10^9$ L mol^{-1} sec^{-1}. Aqueous •OH can readily abstract H• from CH_3CH_2OH to generate aqueous •$CHCH_3OH$ and H_2O. The resulting aqueous •$CHCH_3OH$ can then be adducted to DMPO to yield aqueous DMPO-$CHCH_3OH$.[93] In this context, the aforementioned DMPO-containing aqueous reaction mixtures were further mixed excessive CH_3CH_2OH, stirred vigorously, and filtered to isolate the corresponding aqueous reaction solutions prior to their EPR spectroscopy experiments. The resulting EPR spectra were curve-fitted to bunched signal sets indexed to aqueous DMPO-OH, aqueous DMPO-OOH, and aqueous HDMPO-OH adducts alongside with additional sextet-signal sets with intensity ratio of 1:1:1:1:1:1 assigned to the aqueous DMPO-$CHCH_3OH$ adducts (Fig. S19† and Table S14-S15†).[94] As noted above, aqueous •OH can react with both DMPO and HDMPO to produce aqueous DMPO-OH and HDMPO-OH (Fig. 6A-6B), respectively, whose contents should thus be combined to compare aqueous •OH productivities of the catalysts. If aqueous DMPO-OH arose primarily from aqueous •OH yielded via catalytic H_2O_2 homolysis, the sum of aqueous DMPO-OH and HDMPO-OH contents should decrease substantially upon the addition of CH_3CH_2OH (a potent •OH scavenger) in the reaction mixture subjected to filtration. This claim held true across all quantitative results for the CH_3CH_2OH-bearing EPR spectra of the reaction solutions simulated (Table S13† and S15†; *e.g.*, 88.9 % without CH_3CH_2OH; 40.7 % with CH_3CH_2OH for R600). Moreover, if aqueous DMPO-OH originated predominantly from aqueous •OH produced via H_2O_2 homolysis on the catalyst surface, the sum of aqueous DMPO-OH and HDMPO-OH contents with CH_3CH_2OH being absent in the reaction solution should be comparable to that of aqueous DMPO-OH, HDMPO-OH, and DMPO-$CHCH_3OH$ contents with CH_3CH_2OH being present in the reaction solution. This relationship was consistently observed across all quantitative results for the CH_3CH_2OH-bearing EPR spectra of the reaction solutions simulated (Table S13† and S15†; *e.g.*, 88.9 % without CH_3CH_2OH; 87.3 % with CH_3CH_2OH for R600). These results substantiated that aqueous DMPO-OH primarily stemmed from aqueous •OH generated via catalytic H_2O_2 homolysis rather than DMPO-OOH decomposition. This was in line with previous literatures to argue minimal conversion of aqueous DMPO-OOH to aqueous DMPO-OH (≤ 3 %) under circum-neutral, aqueous pH domains.[91, 92] Overall, all the results on the filtration/diffusion/scavenging runs and the EPR spectra of the

View Article Online DOI: 10.1039/D6TA01370B

aqueous reaction solutions validated -$r_{H2O2,\ 0,\ CO2}$~-$r_{ACETAMINOPHEN,\ 0,\ CO2}$ as well as the rate law dictated mainly by BA^--H^+ features of the catalysts (Eqn. 10-12).

To ensure the obedience of the catalysts to Arrhenius behavior, the catalysts were subjected to acetaminophen degradation runs identically to the diffusion runs except for the alteration of $T_{REACTION}$ values from 25 to 55 °C.[19-22] The resulting -$r_{ACETAMINOPHEN,\ 0,\ CO2}$ values of the catalysts were higher at greater $T_{REACTION}$ values (~0.02 min^{-1}→~0.07 min^{-1} for O300; ~0.02 min^{-1}→~0.06 min^{-1} for R300; ~0.09 min^{-1}→~0.13 min^{-1} for R600 at $T_{REACTION}$ of 25 °C→55 °C), which proved their conformity of Arrhenius law (Fig. S20† and Table S10†).[19-22] Arrhenius plots of logarithmic -$r_{ACETAMINOPHEN,\ 0,\ CO2}$ (ln (-$r_{ACETAMINOPHEN,\ 0,\ CO2}$)) *versus* reciprocal of $T_{REACTION}$ ($1/T_{REACTION}$) were constructed for the catalysts (Eqn. 13/S9†). The resulting slopes and y-intercepts served to assess $E_{BARRIER}$ and k_{APP}' values required to activate H_2O_2 homolysis on the catalyst surfaces. Again, $E_{BARRIER}$ and k_{APP}' values were governed by $E_{BA^-H^+}$ (O300≤R300<R600; $E_{BA^-H^+}$↑→$E_{BARRIER}$↓) and $N_{BA^-H^+}$ values (R600<R300~O300; $N_{BA^-H^+}$↑→k_{APP}'↑), respectively, for the catalysts (Eqn. 12).[19-22]

$$\ln(-r_{POLLUTANT,\ 0,\ CO2}) = \ln(\overbrace{(\frac{k_5' K_1 K_2 K_3 K_4 [S_1]_0 C_{H2O2,\ 0}}{C_{POLLUTANT,\ 0}})}^{y\ -\ intercept} \times C_{POLLUTANT,\ 0}) + \overbrace{(\frac{-E_{BARRIER}}{R})}^{slope} \times \frac{1}{T_{REACTION}} \quad (13)$$

The catalysts exhibited $E_{BARRIER}$ values in the order of R600 (10.8 kJ mol^{-1})<R300~O300 (33.3-34.5 kJ mol^{-1}) and k_{APP}' values in the order of R600 ($5.9X10^{-1}$ min^{-1})<R300~O300 ($3.4X10^3$-$6.1X10^3$ min^{-1}; Fig. 7A). This proved that $E_{BARRIER}$ could override k_{APP}' in determining -$r_{H2O2,\ 0,\ CO2}$ values, enabling R600 to display the highest activity among the catalysts (*vide supra*). This finding highlighted the centrality of H_2 reduction conditions in tuning the acidic strength ($E_{BA^-H^+}$) of the major H_2O_2 activator (BA^--H^+) proper to desorb •OH with lower energy input under optical energy-free, aqueous conditions.

H_2O_2 homolysis on the catalysts: reusability, poison tolerance, and regenerability

To inspect recyclabilities of the catalysts in acetaminophen degradation, recycle runs were performed identically to the diffusion runs except for exposure of the (used) catalysts to acetaminophen disintegration conditions multiple times. After each reaction run, the used catalysts were rinsed with de-ionized H_2O and dried overnight at 110 °C prior to the commencement of the subsequent runs (Fig. S21† and Table S10†).[19-22] As anticipated, -$r_{ACETAMINOPHEN,\ 0}$ values of the catalysts were gradually reduced over successive cycles (Fig. 7B). This could be ascribed to oligomeric by-products yielded via aqueous •OH-enabled addition to or H• abstraction from acetaminophen. These oligomers rich in e^--donating groups can interact with H_2O_2 activators of BA^--H^+ and LA_{II} sites via pseudo-hydrogen bonding and coordination, respectively, thereby hindering their access to aqueous H_2O_2.[21, 37-39]

For this investigation, the reaction solutions subjected to the 1st recycle runs were examined using ultra-performance liquid chromatography equipped with mass spectrometry (UPLC-MS) in positive mode. The UPLC-MS spectra of the reaction solutions were then used to identify intermediates based on their mass (m)/charge (z) values (Fig. S22†).[19-22, 95-97] Aside from revealing acetaminophen (m/z of 152), the UPLC-MS spectra showed several intermediates formed via •OH-mediated addition/H• abstraction or H^+/e^--enabled addition. The latter could proceed with the use of bountiful H^+ and e^- produced at the anode via two H_2O oxidation pathways (H_2O→$2H^+$+$1/2O_2$+$2e^-$ and H_2O→H^++•OH+e^-).[19-22] Most of the intermediates monitored were oligomeric species except for those with m/z values of 91, 100, and 110. The oligomers possessed functional groups of -OH/-NH-/-NH_2 with m/z values of 227, 259, 301, 307, 323, 408, and 450.[19-22]

To further prove catalyst deactivation, Ti and C/N contents of the used catalysts collected post the 1st, 3rd, and 5th recycle runs were evaluated using ICP-AES and elemental analysis (EA), respectively, with which bulk atomic ratios of C to Ti (C/Ti) and N to Ti (N/Ti) could be compared for the used catalysts (Fig. 8C-8D and Table S2†). The C/Ti values were similar across the used catalysts at each of the recycle runs, yet, increased steadily throughout the recycle runs (~$2.6X10^{-1}$ mol_C mol_{Ti}^{-1}→~$3.5X10^{-1}$ mol_C mol_{Ti}^{-1}). This trend indicated progressive accumulation of oligomers on BA^--H^+/LA_{II} sites of the used catalysts and could justify the gradual decline in their -$r_{ACETAMINOPHEN,\ 0}$ values throughout the recycle runs. Moreover, the N/Ti values of used O300 continuously increased throughout the recycle runs (~$10.0X10^{-3}$ mol_N mol_{Ti}^{-1}→~$17.8X10^{-3}$ mol_N mol_{Ti}^{-1}). This was partially the case with the N/Ti values of used R300, whose magnitude was ~$8.5X10^{-3}$ mol_N mol_{Ti}^{-1} prior to the 4th run and reached ~$13.7X10^{-3}$ mol_N mol_{Ti}^{-1} post the 5th run. In contrast, the N/Ti values of used R600 were negligible prior to the 4th run and only ~$3.8X10^{-3}$ mol_N mol_{Ti}^{-1} post the 5th run. The catalysts showed the trend on $E_{BA^-H^+}$ or E_{LAII} values of O300≤R300<R600, suggesting that the extent of oligomer deposition ($N_{OLIGOMER}$) could increase in the identical order.[21, 37-39] However, this was opposite to the trend on N/Ti ($N_{OLIGOMER}$) values for the used catalysts (used R600<<used R300<used O300), demonstrating that oligomer accumulation on BA^--H^+/LA_{II} sites of the used catalysts was not governed solely by their $E_{BA^-H^+}$/E_{LAII} values. Instead, considering the N_{LAII}/$N_{BA^-H^+}$ values of the catalysts (O300~R300~R600 for N_{LAII}; R600<R300~O300 for $N_{BA^-H^+}$), (used) R600 with the smallest $N_{BA^-H^+}$ could detour oligomer deposition more effectively than (used) O300 or (used) R300. Consequently, (used) R600 revealed the highest -$r_{ACETAMINOPHEN,\ 0}$ values among the (used) catalysts over successive recycle runs (Fig. 7B).

Again, •OOH bound to BA^--H^+/LA_{II} sites (poison I) and $O_2^{\bullet-}$ bound to LA_{II} sites (poison II) can severely limit H_2O_2 access to these sites (Fig. 8A).[21, 34] Moreover, H_2O_2 dehydrogenation can generate O_2 covalent-bonded to two vicinal LA_I sites (poison III). These LA_I sites could be located near H_2O_2 activators (BA^--H^+/LA_{II} sites) and therefore impede H_2O_2 distortion and dissection, as conjectured based on N_{LAII}<N_{LAI}<<$N_{BA^-H^+}$ for the catalysts (Fig. 8A).[34-36] Notably, formation of poison II requires cleavage of the pseudo-hydrogen bond between BA^- of BA^--H^+ and the H atom of •OOH (poison I). However, this pathway was expected to be limited across the catalyst surfaces because of $E_{BA^-H^+}$<E_{LAII} (*i.e.*, cleavage of the covalent bond between LA_{II} and the O atom of

View Article Online
DOI: 10.1039/D6TA01378B

•OOH in advance of cleavage of the pseudo-hydrogen bond between BA^- of BA^--H^+ and the H atom of •OOH).[21, 34] Moreover, poison I can bind more strongly with BA^--H^+ or LA_{II} at a lower $E_{BA^-H^+}$ or a lower E_{LAII}, whereas its surface coverage ($N_{POISON\ I}$) can increase with a larger $N_{BA^-H^+}$ or a larger N_{LAII}.[21] Considering the trends on $E_{BA^-H^+}/E_{LAII}$ values of O300≤R300<R600, $N_{BA^-H^+}$ values of R600<R300~O300, and N_{LAII} values of O300~R300~R600, resistance to poison I ($N_{POISON\ I}\downarrow$) was speculated to increase in the order of O300≤R300<R600. Similarly, poison III bind more firmly to LA_I at a lower E_{LAI}, while its accumulation ($N_{POISON\ III}$) can increase at a larger N_{LAI}.[21] Considering the trends on E_{LAI} values of O300<R300<R600 and N_{LAI} values of R600<R300~O300, tolerance to poison III ($N_{POISON\ III}\downarrow$) was expected to increase in the order of O300≤R300<R600. For inspecting the aforestated hypotheses, the catalysts were mixed with aqueous H_2O_2 and ground with a mortar and pestle to yield H_2O_2 activation-subjected, wet catalysts for Raman spectroscopy experiments. The resulting Raman spectra were curve-fitted to five Raman-active bands indexed to E_g or A_{1g}/B_{1g}.[51, 52] The locations of the E_g bands (O300~R300>R600) and their FWHM values (O300~R300>R600) were consistent with those of the H_2O_2 activation-unsubjected, dry catalysts (Fig. 2F-2J/S23† and Table S3/S16†). This indicated that the N_{LAI}/N_{LAII} hierarchies of O300~R300>R600 were retained post their H_2O_2 activation.[51-54] Interestingly, additional Raman-excited bands appeared in the H_2O_2 activation-subjected, wet catalysts with Raman shifts centered at 856-871 cm^{-1}. These bands could be ascribed to photon-excited stretching vibrations of O-O bonds for O_{PEROXY} species (O_{PEROXY}). Although their intensities were lower relative to those of the E_g bands (*; Fig. S23†), their presence was seemingly indispensable, as postulated based on literatures to explore O_{PEROXY} bands via Raman spectroscopy.[98, 99] Notably, the O_{PEROXY} band for wet R600 exhibited a red-shift of ~15 cm^{-1} relative to those for wet O300 and R300. This could partially result from elongation of O-O bonds in O_{PEROXY} species on wet R600 surface, which might arise from its higher $E_{LAII}/E_{BA^-H^+}$ values (O300~R300<R600) for poison I or its higher E_{LAI} values (O300<R300<R600) for poison III.[51-54] Moreover, the area ratio of the O_{PEROXY} band to the E_g band (marked with *; Fig. S23†) was higher for wet O300/R300 (0.07-0.08) than for R600 (0.05). This proved that R600 could exhibit greater resistance to poison I/III accumulation than O300/R300.

To further examine the hypotheses set earlier, the catalysts underwent H_2O_2 dissection runs identically to the 1st recycle runs except for the exclusion of acetaminophen from aqueous reaction solutions and the absence of an electric input applied. The latter was compensated by the inclusion of H_2O_2 in aqueous reaction solutions. Notably, C_{H2O2} was set to 4.1X10^{-3} mol_{H2O2} L^{-1}, corresponding to averaged C_{H2O2} at ≥5 minutes in H_2O_2 evolution runs (Fig. S17†) with a target to simulate the aqueous electric conditions used to carry out the 1st recycle runs (Fig. 7B). The catalysts subjected to H_2O_2 dissection runs were collected via filtration, dried at 110 °C for an hour, and analyzed via XP spectroscopy to explore the type or contents of surface O species (Fig. 8B and Table S17†). The XP spectra of the H_2O_2 dissection-subjected catalysts in the O 1s regimes were curve-fitted into four sub-bands, three of which were assigned to $O_{LATTICE}$, $O_{CHEMISORBED}$, and $O_{BRÖNSTED}$ species with their peak locations (binding energies) being identical to those of the H_2O_2 dissection-unsubjected catalysts.[57-60] This highly suggested that the trends on $E_{BA^-H^+}/E_{LAII}/E_{LAI}$ and $N_{BA^-H^+}/N_{LAII}/N_{LAI}$ values of the catalysts were maintained post undergoing H_2O_2 dissection runs. However, O300 showed a decrease in its $O_{BRÖNSTED}$ content (24.7 %→18.6 %), whereas only minor changes were observed for R300 (12.7 %→10.7 %) and R600 (6.2 %→5.2 %). This substantiated that poison I deposition on BA^--H^+/LA_{II} sites was unavoidable in O300 surface and was unlikely in R300 and R600 surfaces. Similarly, $O_{CHEMISORBED}$ content decreased substantially for O300 (24.5 %→11.2 %) and R300 (24.1 %→12.4 %), yet, remained almost unaltered for R600 (6.0 %→5.5 %). This demonstrated that poison III deposition on LA_I sites was imperative in O300 and R300 surfaces and was minimal in R600 surface.

The remaining sub-bands of the XP spectra in the O 1s regions could be indexed to O of Ti-peroxy species (poison I or III; O_{PEROXY}) with binding energies centered at 533.0-533.4 eV.[21] Notably, the binding energies of O_{PEROXY} species inherent to H_2O_2 dissection-subjected R300 and R600 were 0.4 eV higher than that innate to H_2O_2 dissection-subjected O300 (533.0 eV). This shift could be justified by differences in E_{LAI} (O300<R300<R600) and N_{LAI} values (R600<R300~O300), both of which were lumped, as discussed earlier.[25, 55, 56] Hence, e^- donation from the O atom of poison III to proximal LA_I sites could be more pronounced for R300/R600 than for O300. Nevertheless, the O_{PEROXY} contents were substantially higher for H_2O_2 dissection-subjected O300 and R300 (17.8-18.6 %) than for H_2O_2 dissection-subjected R600 (3.3 %), which was in agreement with the trend on their $O_{CHEMISORBED}$ contents directed by poison III accumulation on LA_I sites of the catalysts subjected to H_2O_2 dissection runs. Overall, R600 with the smallest $N_{BA^-H^+}$, highest $E_{BA^-H^+}$, and highest E_{LAI} showed the strongest reluctance to accumulation of oligomeric species, poison I, and poison III, respectively, upon exposure to aqueous organic degradation conditions.

Albeit with validation concerning the superiority of R600 to O300 and R300 in tolerating oligomeric species and poison I/III, their regenerabilities to sustain H_2O_2 homolysis remained unexamined. (used) O300 and (used) R600 were thus chosen because of their similar resuabilities and poisoning patterns (Fig. 7B/8/S21† and Table S17†). The $-r_{ACETAMINOPHEN,\ 0,\ CO2}$ values of (used) O300 and R600 were then monitored over extended recycle runs up to the 10th cycles (Fig. 9/S24† and Table S10†). $-r_{ACETAMINOPHEN,\ 0,\ CO2}$ values of O300 and R600 were continuously declined, whereas $-r_{ACETAMINOPHEN,\ 0,\ CO2}$ values of the latter were 1.2-2.3-fold higher than those of the former at each of the recycle runs, clearly demonstrating that R600 outstripped O300 in sustaining •OH production via H_2O_2 homolysis.

The R600 and O300 collected post being subjected to the 10th cycle were further examined with the use of thermo-gravimetric analysis (TGA) technique, with which profiles of weight percent (wt. %) *versus* temperature under a N_2 were recorded (Fig. S25†). The decrease in wt. % monitored for used O300 and R600 corresponded to 11.4 wt. % and 4.5 wt. %, respectively, at 110-800 °C. This verified greater resistance to

View Article Online
DOI: 10.1039/D6TA01339B

oligomeric poison or poison I/III deposition was achievable for R600 rather than for O300, while supporting greater recyclability of R600 in activating H_2O_2 homolysis compared to that of O300.

Moreover, the used catalysts exhibited continuous weight loss at 110-800 °C, where H_2O molecules chemisorbed on LA_I/LA_{II} sites could be desorbed at 110-400 °C, whereas acetaminophen (or its oligomeric derivative) and poison I/III (O_{PEROXY}) could be pyrolyzed or desorbed at 200-350 °C and at 110-170 °C, respectively. This was postulated given a spectrum of literatures on pyrolysis or desorption of H_2O, acetaminophen, and O_{PEROXY} via TGA under inert environments.[100-103] Considering thermal behaviors of the aforementioned species and considering the synthetic conditions of O300 (air; 300 °C) and R600 (H_2; 600 °C), the used catalysts were regenerated under a N_2 at 300 °C for 4 hours to restore their surface acidic features. The catalysts subjected to regeneration were then reevaluated under acetaminophen degradation environments. The resulting -$r_{ACETAMINOPHEN,\ 0,\ CO2}$ values were recovered to around 70 % of those in the 1st cycle of the recycle runs (Fig. 9/S24† and Table S10†). This highly suggested a fraction of oligomeric poisons or poison I/III could be pyrolyzed under inert conditions.

The catalysts subjected to the 10th cycle or regeneration were further characterized by XP spectroscopy to explore their surface properties. The XP spectra in the O 1s regimes revealed such O_{PEROXY} contents as to be around 3-fold higher in used O300 (32.6 %) than in used R600 (Fig. S26† and Table S18†). This was in accordance with the trends on -$r_{ACETAMINOPHEN,\ 0,\ CO2}$ values (Fig. 9), wt. % loss (via TGA; Fig. S25†), surface C/Ti ratios (2.3 for used O300; 1.4 for used R600), and surface N/Ti ratios (0.26 for used O300; 0.11 for used R600) for the used catalysts (Table S18†). Nonetheless, O_{PEROXY} contents of the used catalysts were marked reduced to nearly 0 % post their regeneration. This indicated that residual oligomeric poisons remained on the used catalyst surfaces even after regeneration. This was also proved by only partial recovery of $O_{BRÖNSTED}$/$O_{CHEMISORBED}$ contents (~9.8 % for recovered O300), surface C/Ti ratios (1.5 for recovered O300), and surface N/Ti ratios (0.15 for recovered O300) for the used catalysts in comparison with those of the corresponding catalysts as-synthesized ($O_{BRÖNSTED}$/$O_{CHEMISORBED}$ of ~24.6 %, C/Ti of ~0, and N/Ti of ~0 for as-synthesized O300; Table S17-S18†). Nevertheless, surface C/Ti and N/Ti values were higher in recovered O300 than in regenerated R600 (C/Ti of 1.1 and N/Ti of 0.07 for recovered R600; Table S18†). This corroborated that R600 outstripped O300 and R300 in sustaining repeated H_2O_2 homolysis and in restoring acidic features desired to activate H_2O_2 homolysis.

H_2O_2 homolysis on the catalysts: DFT calculations

To further justify our findings on poison resistance for the catalysts, density functional theory (DFT) calculations were carried out according to methodologies specified in the Supplementary Information†. A TiO_2 (anatase) slab was initially terminated on its major (101) facet (evidenced by XRD patterns; Fig. S2†) and subjected to geometric optimization, upon which a fraction of *hexa*-fold coordinated, defect-free Ti atoms transformed into *penta*-fold coordinated analogues (LA_I) alongside with the impartation of BA^--H^+ sites (Fig. 10A; surface I).

Poison III (O_2) was first attempted to undergo chemisorption on two adjacent LA_I sites of surface I, yet, did not converge to a stable local energy minimum. This could stem from *octahedral* $[Ti^{4+}\text{-}(O^{2-})_6]^{8-}$ sub-units of TiO_2 lattice (Fig. 1B), whose geometric energy minimum is contingent upon stable coordination of each Ti^{4+} center with six O^{2-} anions (*i.e.*, one for O_2 (poison III); five for O^{2-} anions; Fig. 10B). Nonetheless, it should not be disregarded that poison III could settle stably down to dynamic TiO_2 surface facets via formation of covalent bonds with two adjacent LA_I sites (Fig. 8A).[3, 34-36] In contrast, poison III adsorption on a single LA_I site on surface I was computed to be feasible, as boosted by the change in thermodynamic energy involved ($\Delta E_{ADSORPTION}$ (O_2) of -6.8 kJ mol^{-1}; Fig. 10B), proving the significance of poison III as a potential surface contaminator.

Moreover, an O atom positioned between two LA_I sites on surface I was removed to yield an O_V and two *tetra*-fold coordinated Ti centers (LA_{II}) in resulting surface II (Fig. 10D). Upon relaxation, the LA_{II} sites moved away from the O_V and revealed LA_{II}-O bond lengths of 2.04 Å (i), 1.96 Å (ii), and 1.88 Å (iii) (Fig. 10D). In particular, one of LA_{II}-O bond lengths (ii) was 0.04 Å shorter than the corresponding LA_{II}-O bond on surface I (2.00 Å; Fig. 10A), validating geometric distortion of $[Ti^{4+}\text{-}(O^{2-})_6]^{8-}$ sub-units was highly likely, as discussed earlier (Fig. 1B).[3] Meanwhile, Bader charges of LA_I (*n* of 5) and LA_{II} (*n* of 4) sites on surface II were computed for comparison with that of defect-less Ti center (*n* of 6). Bader charges were elevated in the sequence of LA_{II}<LA_I<defect-free Ti (Fig. 10C), substantiating the quantity of e^- trapped near the sub-shells of LA_{II} site was greater than that of either LA_I site or defect-less Ti center, as stated earlier (Fig. 1C).[1, 19-24]

Surface II experienced •OH and poison I (•OOH) adsorption on BA^--H^+/LA_{II} sites (Fig. 10E-10F). The likelihood of •OH adsorption was of energetic spontaneity, as proved by the change in thermodynamic energy involved ($\Delta E_{ADSORPTION}$ (•OH) of -209.4 kJ mol^{-1}), whereas the likelihood of poison I adsorption was of energetic unspontaneity, as evidenced by the change in thermodynamic energy involved ($\Delta E_{ADSORPTION}$ (•OOH) of 114.8 kJ mol^{-1}). Again, it should be stressed that surface facets of poly-crystalline TiO_2 were highly entangled to facilitate H_2O_2-mediated •OH transition to poison I on BA^--H^+/LA_{II} sites (Fig. 8A).[21, 34] Notably, in •OH-bound surface II (Fig. 10E), the bond between BA^- of BA^--H^+ and the H atom of •OH (v) was 0.44 Å shorter than that between LA_{II} and the O atom of •OH (iv), proving $E_{BA^-\text{-}H^+}$<E_{LAII} for the catalyst surfaces in conjunction with the centrality of BA^--H^+ functioning as the primary activator of H_2O_2 homolysis. In addition, albeit with energetic instability of •OOH-bound surface II (Fig. 10F), the bond between BA^- of BA^--H^+ and the H atom of •OOH (vii) was 1.09 Å shorter than that between LA_{II} and the O atom of •OOH (vi), indicating that bond strength was higher in vii than in vi. This could support the unlikelihood of poison I (•OOH)-induced formation of poison II ($O_2^{\bullet-}$) on LA_{II} sites (Fig. 8A) because bond vii should be cleaved to yield poison II.[21, 34] Indeed, the change in thermodynamic energy involved in poison II adsorption on two LA_{II} sites (not a single LA_{II}; due to marked stability of $[Ti^{4+}\text{-}(O^{2-})_6]^{8-}$ sub-units;

View Article Online DOI: 10.1039/D6TA01373B

vide supra) was computed to be 93.6 kJ mol^{-1} ($\Delta E_{ADSORPTION}$ ($O_2^{\bullet-}$); Fig. 10G), further demonstrating poison II could scarcely be deposited on the catalyst surfaces.

H_2O_2 homolysis on the catalysts: adaptability

To examine the adaptabilities of the catalysts in disintegrating aqueous organics, acetaminophen, bisphenol A, aniline/phenol, and sulfanilamide/sulfmethoxazole were selected as model compounds representing an analgesic, endocrine disruptor, pesticide, and antibiotic, respectively (Fig. 11A).[14, 21, 22, 37] These compounds contain distinct combinations of e^--donating groups (-OH/-NH-/-NH_2) and e^--withdrawing groups (-SO_2-) and thereby reveal dissimilar energies needed to deprive -OH/-NH-/-NH_2 of e^- (ionization potential; Table S19†).[76-78] Accordingly, the -$r_{POLLUTANT,\ 0,\ CO2}$ values of the catalysts should scale inversely with the ionization potentials of the pollutants, if their degradation primarily proceeded via (H^+-coupled) e^- transfer on ROS (*e.g.*, $H_2PO_4^{\bullet}$, $Cl^{\bullet}$, or Fe^{IV}=O).[14, 21, 22, 37] However, the catalysts elaborated herein could produce $^{\bullet}$OH implemented to fragment contaminants primarily via addition or $^{\bullet}$H abstraction. Hence, the -$r_{POLLUTANT,\ 0,\ CO2}$ values were expected to show little correlation with the ionization potentials of the pollutants.[14, 21, 22, 37]

The catalysts underwent contaminant degradation runs identically to the diffusion runs except for the replacement of acetaminophen with those listed earlier and the adjustment of initial concentration for bisphenol A to 0.4X10^{-4} $mol_{BISPHENOL\ A}$ L^{-1} with the consideration of its aqueous solubility (Fig. S27† and Table S10†).[14, 19-22, 37, 104, 105] Moreover, kinetic datasets with $X_{POLLUTANT}$ values of <30 % were considered to precisely assess k_{APP} values of the catalysts, while ensuring the equilibrium of pollutant degradation (or H_2O_2 homolysis) was effectively driven forward at $T_{REACTION}$ of 25 °C.[14, 19-22, 37] The -$r_{POLLUTANT,\ 0,\ CO2}$ values of the catalysts revealed little correlation with the ionization potentials of the corresponding pollutants. This was demonstrated by the poor linear fits (R^2<0.1) obtained from plots of -$r_{POLLUTANT,\ 0,\ CO2}$ *versus* ionization potential (Fig. 11C).[14, 21, 22, 37] This indicated that the catalysts deployed $^{\bullet}$OH as the major decomposer of aqueous pollutants under the electric conditions, as also demonstrated by the scavenging runs and EPR spectroscopy experiments (Fig. 5B and 6). Importantly, the -$r_{POLLUTANT,\ 0,\ CO2}$ values of R600 were around 2-17-fold and 3-23-fold higher than those of O300 and R300, respectively (Fig. 11B). The -$r_{POLLUTANT,\ 0}$ values and extent of active metal cation (Ti^{4+}) leaching for R600 were further compared with those of ZrO_2 (or Zr-based metal-organic framework; UiO-66) and Fe_2O_3 (or Fe_3O_4) we studied elsewhere[20, 22, 106] ZrO_2/UiO-66 and Fe_2O_3/Fe_3O_4 can produce $^{\bullet}$OH via H_2O_2 homolysis and H_2O_2 heterolysis ($H_2O_2+e^-\rightarrow{}^{\bullet}OH+OH^-$), respectively, under the electric conditions (Table S20†).

Despite negligible Ti^{4+}/Zr^{4+} leaching (~10^{-4} mol. %), the -$r_{POLLUTANT,\ 0}$ values of R600 were around 3-10-fold higher than those of ZrO_2 (or UIO-66).[20, 22] In addition, the number of Ti^{4+} cations released from R600 was 3 orders of magnitude smaller than that of $Fe^{2+/3+}$ cations liberated from Fe_2O_3 (or Fe_3O_4; ~10^{-1} mol. %) in bisphenol A degradation runs, albeit the -$r_{BISPHENOL\ A,\ 0}$ values were comparable.[106] Overall, these results corroborated the superiority of R600 to O300/R300 or ZrO_2/UiO-66/Fe_2O_3/Fe_3O_4 in disintegrating refractory organic wastes under optical energy-free, aqueous media.

Conclusions

TiO_2 subjected to thermal H_2 reduction generates BA^--H^+ and LA_I/LA_{II} sites. The latter create intra-bandgap states (INTRA) that localize e^- near the valence band (VB) to bear h^+ with h^+ and e^- being photo-excited to produce $^{\bullet}$OH, $O_2^{\bullet-}$, or $^1O_2$ (ROS) via semi-conducting routes. However, control over the type of ROS generated through selective acceleration of these pathways remains challenging. This is because E_{INTRA} and E_{VB} rely highly on aqueous pH range and because the narrow optical energy gap of E_{INTRA}-E_{VB} can limit the range of accessible optical transitions, thereby restricting the number of ROS production pathways that can be activated.

Alternatively, non-optical H_2O_2 homolysis ($H_2O_2\rightarrow 2^{\bullet}OH$) was envisioned as a route to deploy BA^--H^+ and LA_{II} sites on H_2-reduced TiO_2. These sites proceed with H_2O_2 adsorption, H_2O_2 distortion, H_2O_2 dissection, and $^{\bullet}$OH desorption (RDS) with a greater N_{BA-H+} (or N_{LAII}) and a higher E_{BA-H+} (or E_{LAII}) favoring k_{APP}' elevation and $E_{BARRIER}$ reduction, respectively, for promoted $^{\bullet}$OH productivity. In this regard, TiO_2 experienced O_2 calcination at 300 °C and H_2 reduction at 300-600 °C to produce O300 and R300-R600, respectively, all of which revealed acidic trends of N_{LAII}<N_{LAI}<<N_{BA-H+} and E_{BA-H+}<E_{LAI}~E_{LAII}. This made it compelling that H_2O_2 consumption rate (-r_{H2O2}) law could hinge on N_{BA-H+}/E_{BA-H+} rather than on N_{LAII}/E_{LAII}. Meanwhile, -r_{H2O2} is challenging to directly monitor owing to short life-span of $^{\bullet}$OH (~10^{-3} μsecond) and thereby was assessed using background-corrected -$r_{ACETAMINOPHEN,\ 0,\ CO2}$ and/or -$r_{ACETAMINOPHEN,\ 0}$. This approach was supported by the minute LA_{II} leaching, the absence of internal/external mass-transfer limitations for $H_2O_2\leftrightarrow BA^-$-$H^+$/$LA_{II}$ and $^{\bullet}$OH↔acetaminophen interactions, and the identification of $^{\bullet}$OH (rather than $^{\bullet}$OOH/$O_2^{\bullet-}$) as the primary ROS responsible for acetaminophen decomposition.

In particular, O300, R300, and R600 were distinct and tunable in terms of acidic traits such as R600<R300~O300 for N_{BA-H+}, O300~R300~R600 for N_{LAII}, and O300≤R300<R600 for E_{BA-H+}/E_{LAII}, in conjunction with H_2O_2 dissectors (BA^--H^+/LA_{II})-proximal LA_I features of R600<R300~O300 for N_{LAI} and O300<R300<R600 for E_{LAI}. R600 outstripped O300 and R300 in multiple aspects. R600 revealed the lowest $E_{BARRIER}$ and lowest k_{APP}', yet, displayed the highest -$r_{ACETAMINOPHEN,\ 0,\ CO2}$. This indicated $E_{BARRIER}$ outweighed k_{APP}' in directing -$r_{ACETAMINOPHEN,\ 0,\ CO2}$ for TiO_2 subjected to H_2 reduction. R600 also unveiled the greatest tolerance to deposit poisonous oligomer on BA^--H^+/LA_{II} sites, arising from its smallest N_{BA-H+}. In addition, R600 showed the highest resistance to accumulate poisonous $^{\bullet}$OOH on BA^--H^+/LA_{II} sites or poisonous O_2 on LA_I sites, arising from its smallest N_{BA-H+}, highest E_{BA-H+}, and highest E_{LAII} for $^{\bullet}$OOH and its smallest N_{LAI} coupled with highest E_{LAI} for O_2. All of these could be gathered with the DFT calculations to justify the highest -$r_{ACETAMINOPHEN,\ 0}$ values for R600 throughout acetaminophen disintegration recycle runs in conjunction with its moderate recovery upon exposure to regeneration environments.

Furthermore, R600 disclosed the greatest adaptability to fragment diverse aqueous pollutants including an analgesic (acetaminophen), endocrine disruptor (bisphenol A), pesticide (aniline/phenol), and antibiotic (sulfanilamide/sulfmethoxazole). This was corroborated by - $r_{POLLUTANT,\ 0,\ CO2}$ values of R600 that were 2-23-fold higher than those of O300/R300 and 3-10 fold higher than those of ZrO_2/UiO-66.

Author contributions

Minsung Kim: Methodology, Validation, Data Curation, Writing - Original Draft, Formal analysis, Investigation, Visualization. **Gyuchan Kim**: Methodology, Validation, Data Curation, Writing - Editing, Formal analysis, Investigation, Visualization, Software. **Junseo Kim**: Methodology, Validation, Data Curation, Writing - Editing, Formal analysis, Investigation, Visualization. **Sang Hoon Kim**: Writing - Editing, Resources, Funding acquisition. **Byung-Hyun Kim**: Methodology, Validation, Data Curation, Writing - Original Draft, Investigation, Visualization, Software, Supervision, Resources. **Jongsik Kim**: Conceptualization, Methodology, Validation, Data Curation, Writing - Original Draft, Investigation, Visualization, Supervision, Resources, Project administration, Funding acquisition.

Conflicts of interest

There are no conflicts to declare.

Data availability

The data supporting this article have been included as part of the Supplementary Information.

Acknowledgements

This work was supported by the Korea Institute for Advancement of Technology and the Ministry of Trade, Industry & Energy (RS-2026-25509542). This study was conducted with the support of the equipment and facilities provided by the ACE Center at Kyung Hee University. We are thankful to the Korea Institute of Science and Technology for supporting this project through Future R&D.

References

1. V. K. Paidi, B.-H. Lee, D. Ahn, K.-J. Kim, Y. Kim, T. Hyeon and K.-S. Lee, *Nano Lett.*, 2021, **21**, 7953-7959.
2. J. Chapman, K. E. Kweon, Y. Zhu, K. Bushick, L. B. Bayu Aji, C. A. Colla, H. Mason, N. Goldman, N. Keilbart, S. R. Qiu, T. W. Heo, J. Rodriguez and B. C. Wood, *J. Mater. Chem. A*, 2023, **11**, 8670-8683.
3. D. Van den Eynden, R. Pokratath and J. De Roo, *Chem. Rev.*, 2022, **122**, 10538-10572.
4. Ľ. Benco, J.-L. Barras, C. A. Daul and E. Deiss, *Inorg. Chem.*, 1999, **38**, 20-28.
5. Z.-W. Qu and G.-J. Kroes, *J. Phys. Chem. B*, 2006, **110**, 8998-9007.
6. J. Shim, K. Lee, Y. Yu, H. S. Lee, H. Shin, K.-S. Lee, M. S. Bootharaju, S. Han, G. S. Yi, H. Ko, S. Lee, J. Ryu, M. Kim, B.-H. Lee, T. Hyeon and Y.-E. Sung, *J. Am. Chem. Soc.*, 2025, **147**, 16179-16188.
7. B. Ji, J. Gou, Y. Zheng, X. Pu, Y. Wang, P. Kidkhunthod and Y. Tang, *Adv. Mater.*, 2023, **35**, 2300381.
8. H. Song, W. Xie, Y. Tian, M. Guo, T. Wang, D. Kang, M. Jia and X. Zhang, *J. Mater. Chem. A*, 2024, **12**, 15154-15162.
9. L. Jing, B. Xin, F. Yuan, L. Xue, B. Wang and H. Fu, *J. Phys. Chem. B*, 2006, **110**, 17860-17865.
10. M. S. Hamdy, R. Amrollahi and G. Mul, *ACS Catal.*, 2012, **2**, 2641-2647.
11. S. Oh, J.-H. Kim, H. M. Hwang, D. Kim, J. Kim, G. H. Park, J. S. Kim, Y. H. Lee and H. Lee, *J. Mater. Chem. A*, 2021, **9**, 4822-4830.
12. A. J. Hoffman, E. R. Carraway and M. R. Hoffmann, *Environ. Sci. Technol.*, 1994, **28**, 776-785.
13. X. Li, C. Chen and J. Zhao, *Langmuir*, 2001, **17**, 4118-4122.
14. M. Kim, H. Lee, J. Kim, H. Yu, T. Yu, K. Jeong and J. Kim, *J. Alloys Compd.*, 2024, **1008**, 176782.
15. W. He, H.-K. Kim, W. G. Wamer, D. Melka, J. H. Callahan and J.-J. Yin, *J. Am. Chem. Soc.*, 2014, **136**, 750-757.
16. L. Wang, J. Li, X. Liu, J. Zhang, P. Zeng and Y. Song, *Chemosphere*, 2023, **324**, 138264.
17. P. Chen, Y. Zhao, C. Li, X. Chen and J. Wang, *J. Mater. Chem. A*, 2025, **13**, 25829-25841.
18. L. Wu, H. Li, W. Wang, S. Zhang, S. Zeng and X. Zhou, *J. Mater. Chem. A*, 2025, **13**, 37008-37017.
19. M. Kim, J. Park, S. H. Kim, J.-H. Lee, K. Jeong and J. Kim, *Carbon*, 2023, **203**, 630-649.
20. Y. J. Choe, S. Lee, M. Kim, S. H. Kim, I.-S. Choi, K. Jeong and J. Kim, *Sep. Purif. Technol.*, 2023, **310**, 123146.
21. J. Kim, M. Kim, B. Y. Woo, S. Byun, G. Bang, K. M. Cho, H. Jung, K. Jeong and J. Kim, *Chem. Eng. J.*, 2025, **519**, 165063.
22. M. Kim, M. Al Mamunur Rashid, Y. J. Choe, S. H. Kim, J.-H. Lee, K. Jeong and J. Kim, *J. Mater. Chem. A*, 2023, **11**, 9436-9454.
23. N. M. Dimitrijevic, Z. V. Saponjic, B. M. Rabatic, O. G. Poluektov and T. Rajh, *J. Phys. Chem. C*, 2007, **111**, 14597-14601.
24. L.-B. Xiong, J.-L. Li, B. Yang and Y. Yu, *J. Nanomater.*, 2012, **2012**, 831524.
25. T. S. Rajaraman, S. P. Parikh and V. G. Gandhi, *Chem. Eng. J.*, 2020, **389**, 123918.
26. B. Bharti, S. Kumar, H.-N. Lee and R. Kumar, *Sci. Rep.*, 2016, **6**, 32355.
27. D. Nanda Gopala Krishna, R. P. George and J. Philip, *J. Phys. Chem. C*, 2021, **125**, 16136-16146.
28. E. Albanese, A. Ruiz Puigdollers and G. Pacchioni, *ACS Omega*, 2018, **3**, 5301-5307.
29. Y. Li, W. Zhang, J. Niu and Y. Chen, *ACS Nano*, 2012, **6**, 5164-5173.
30. Q. Xiang, J. Yu and P. K. Wong, *J. Colloid Interface Sci.*, 2011, **357**, 163-167.
31. Z. Feng, Q. Tian, Q. Yang, Y. Zhou, H. Zhao and G. Zhao, *Appl. Catal. B*, 2021, **286**, 119908.
32. T. D. Gould, A. M. Lubers, B. T. Neltner, J. V. Carrier, A. W. Weimer, J. L. Falconer and J. Will Medlin, *J. Catal.*, 2013, **303**, 9-15.
33. R. Barth, R. Pitchai, R. L. Anderson and X. E. Verykios, *J. Catal.*, 1989, **116**, 61-70.
34. K. Sahel, L. Elsellami, I. Mirali, F. Dappozze, M. Bouhent and C. Guillard, *Appl. Catal. B*, 2016, **188**, 106-112.
35. C. M. Lousada, A. J. Johansson, T. Brinck and M. Jonsson, *J. Phys. Chem. C*, 2012, **116**, 9533-9543.
36. W.-F. Huang, P. Raghunath and M. C. Lin, *J. Comput. Chem.*, 2011, **32**, 1065-1081.
37. M. Kim, S. H. Kim and J. Kim, *Sep. Purif. Technol.*, 2025, **378**, 134563.
38. S. Yu, S. Tong, M. Chen, H. Zhang, Y. Xu, Y. Guo and M. Ge, *Environ. Sci. Technol.*, 2025, **59**, 11666-11676.

39. T.-Y. Liu, C. Wang, Y.-Z. Han, C. Bai, H.-T. Ren, Y. Liu and X. Han, *Chem. Eng. J.*, 2022, **435**, 134816.
40. J. Kim, S. Lee and H. P. Ha, *ACS Catal.*, 2021, **11**, 767-786.
41. S. Bakardjieva, J. Šubrt, V. Štengl, M. J. Dianez and M. J. Sayagues, *Appl. Catal. B*, 2005, **58**, 193-202.
42. W. Zhang, X. Liu, L. Li, Z. Sun, S. Han, Z. Wu and J. Luo, *Chem. Mater.*, 2018, **30**, 4081-4088.
43. S. Kumar, S. Khanchandani, M. Thirumal and A. K. Ganguli, *ACS Appl. Mater. Interfaces*, 2014, **6**, 13221-13233.
44. N. Riaz, F. K. Chong, B. K. Dutta, Z. B. Man, M. S. Khan and E. Nurlaela, *Chem. Eng. J.*, 2012, **185-186**, 108-119.
45. S. Lettieri, V. Gargiulo, M. Alfè, M. Amati, P. Zeller, V.-A. Maraloiu, F. Borbone, M. Pavone, A. B. Muñoz-García and P. Maddalena, *J. Phys. Chem. C*, 2020, **124**, 3564-3576.
46. Y. Zhang, Z. Su, A. K. Azad, W. Zhou and J. T. S. Irvine, *Adv. Energy Mater.*, 2012, **2**, 316-321.
47. S. Jiang, G. Su, J. Wu, C. Song, Z. Lu, C. Wu, Y. Wang, P. Wang, M. He, Y. Zhao, Y. Jiang, X. Zhao, H. Rao and M. Sun, *ACS Appl. Mater. Interfaces*, 2023, **15**, 11787-11801.
48. F. Nekouei, C. J. Pollock, T. Wang, Z. Zheng, Y. Zhang, Z. Fusco, H. Jin, T. R. Ramireddy, A. A. Wibowo, T. Lu, S. Nekouei, F. Keshtpour, J. Langley, E. H. Abdelkader, N. Cox, Z. Yin, H. Nguyen, A. Glushenkov, S. Karuturi, Z. Liu, L. Wei, H. Li and Y. Liu, *ACS Catal.*, 2025, **15**, 1431-1443.
49. N. E. Kochkina, A. V. Agafonov, A. V. Vinogradov, N. S. Karasev, N. L. Ovchinnikov and M. F. Butman, *ACS Sustainable Chem. Eng.*, 2017, **5**, 5148-5155.
50. R. Scotti, I. R. Bellobono, C. Canevali, C. Cannas, M. Catti, M. D'Arienzo, A. Musinu, S. Polizzi, M. Sommariva, A. Testino and F. Morazzoni, *Chem. Mater.*, 2008, **20**, 4051-4061.
51. S. K. Mukherjee and D. Mergel, *J. Appl. Phys.*, 2013, **114**, 013501.
52. H. Li, L. Shen, K. Zhang, B. Sun, L. Ren, P. Qiao, K. Pan, L. Wang and W. Zhou, *Appl. Catal. B*, 2018, **220**, 111-117.
53. X. Yu, B. Kim and Y. K. Kim, *ACS Catal.*, 2013, **3**, 2479-2486.
54. H. C. Choi, Y. M. Jung and S. B. Kim, *Vib. Spectrosc.*, 2005, **37**, 33-38.
55. G. An, W. Ma, Z. Sun, Z. Liu, B. Han, S. Miao, Z. Miao and K. Ding, *Carbon*, 2007, **45**, 1795-1801.
56. R. Katal, M. Salehi, M. H. Davood Abadi Farahani, S. Masudy-Panah, S. L. Ong and J. Hu, *ACS Appl. Mater. Interfaces*, 2018, **10**, 35316-35326.
57. W. Shen, D. Xiang, J. Yang, Y. Tang, C. Xin, Q. Guo and X. Yu, *Colloids Surf. A: Physicochem. Eng. Asp.*, 2022, **653**, 129965.
58. T. Su, Y. Yang, Y. Na, R. Fan, L. Li, L. Wei, B. Yang and W. Cao, *ACS Appl. Mater. Interfaces*, 2015, **7**, 3754-3763.
59. U. Diebold, *Surf. Sci. Rep.*, 2003, **48**, 53-229.
60. C. Sun, L.-M. Liu, A. Selloni, G. Q. Lu and S. C. Smith, *J. Mater. Chem. A*, 2010, **20**, 10319-10334.
61. A. Naldoni, M. Altomare, G. Zoppellaro, N. Liu, Š. Kment, R. Zbořil and P. Schmuki, *ACS Catal.*, 2019, **9**, 345-364.
62. J. Kim, Y. J. Choe, S. H. Kim, I.-S. Choi and K. Jeong, *JACS Au*, 2021, **1**, 1158-1177.
63. J. Sui, M.-L. Gao, C. Liu, Y. Pan, Z. Meng, D. Yuan and H.-L. Jiang, *J. Mater. Chem. A*, 2023, **11**, 18733-18739.
64. A. Vimont, A. Travert, P. Bazin, J.-C. Lavalley, M. Daturi, C. Serre, G. Férey, S. Bourrelly and P. L. Llewellyn, *Chem. Commun.*, 2007, DOI: 10.1039/B703468G, 3291-3293.
65. X. Ma, L. Li, R. Chen, C. Wang, H. Li and S. Wang, *Appl. Surf. Sci.*, 2018, **435**, 494-502.
66. V. Bolis, C. Morterra, B. Fubini, P. Ugliengo and E. Garrone, *Langmuir*, 1993, **9**, 1521-1528.
67. X. Wang, L. Lu, B. Wang, Z. Xu, Z. Xin, S. Yan, Z. Geng and Z. Zou, *Adv. Func. Mater.*, 2018, **28**, 1804191.
68. Y. Guo, C. Tan, J. Sun, W. Li, J. Zhang and C. Zhao, *Chem. Eng. J.*, 2020, **381**, 122736.
69. S. Lee, S. H. Park and J. Kim, *J. Mater. Chem. A*, 2024, **12**, 24574-24592.
70. S. Lee, J. Choi, H. P. Ha, J.-H. Lee, J. Park and J. Kim, *ACS Catal.*, 2024, **14**, 3349-3368.
71. S. H. Park, S. Lee and J. Kim, *J. Hazard. Mater.*, 2025, **484**, 136653.
72. G. Zhan, Y. Hong, F. Lu, A.-R. Ibrahim, M. Du, D. Sun, J. Huang, Q. Li and J. Li, *J. Mol. Catal. A Chem.*, 2013, **366**, 215-221.
73. G. Vega, A. Quintanilla, M. Belmonte and J. A. Casas, *Chem. Eng. J.*, 2022, **428**, 131128.
74. M. P. Murphy, H. Bayir, V. Belousov, C. J. Chang, K. J. A. Davies, M. J. Davies, T. P. Dick, T. Finkel, H. J. Forman, Y. Janssen-Heininger, D. Gems, V. E. Kagan, B. Kalyanaraman, N.-G. Larsson, G. L. Milne, T. Nyström, H. E. Poulsen, R. Radi, H. Van Remmen, P. T. Schumacker, P. J. Thornalley, S. Toyokuni, C. C. Winterbourn, H. Yin and B. Halliwell, *Nat. Metab.*, 2022, **4**, 651-662.
75. J. S. Barroso-Martínez, A. I. B. Romo, S. Pudar, S. T. Putnam, E. Bustos and J. Rodríguez-López, *J. Am. Chem. Soc.*, 2022, **144**, 18896-18907.
76. J. Wang, K.-P. Hou, Y. Wen, H. Liu, H. Wang, K. Chakarawet, M. Gong and X. Yang, *J. Am. Chem. Soc.*, 2022, **144**, 4294-4299.
77. P. Hu, H. Su, Z. Chen, C. Yu, Q. Li, B. Zhou, P. J. J. Alvarez and M. Long, *Environ. Sci. Technol.*, 2017, **51**, 11288-11296.
78. H. Lei and S. A. Snyder, *Water Res.*, 2007, **41**, 4051-4060.
79. J. Kim, Y. J. Choe and S. H. Kim, *Chem. Eng. J.*, 2021, **413**, 127550.
80. S. O. Ganiyu, N. Oturan, S. Raffy, M. Cretin, C. Causserand and M. A. Oturan, *Sep. Purif. Technol.*, 2019, **208**, 142-152.
81. V. K. Parida, S. K. Srivastava, S. Chowdhury and A. K. Gupta, *Chem. Eng. J.*, 2023, **472**, 144969.
82. Q. Mei, J. Sun, D. Han, B. Wei, Z. An, X. Wang, J. Xie, J. Zhan and M. He, *Chem. Eng. J.*, 2019, **373**, 668-676.
83. J. R. Alvarez-Idaboy, N. Mora-Diez, R. J. Boyd and A. Vivier-Bunge, *J. Am. Chem. Soc.*, 2001, **123**, 2018-2024.
84. T. Yasuhisa, H. Hideki and Y. Muneyoshi, *Int. J. Biochem.*, 1993, **25**, 491-494.
85. G. V. Buxton, C. L. Greenstock, W. P. Helman and A. B. Ross, *J. Phys. Chem. Ref. Data*, 1988, **17**, 513-886.
86. B. H. J. Bielski, D. E. Cabelli, R. L. Arudi and A. B. Ross, *J. Phys. Chem. Ref. Data*, 1985, **14**, 1041-1100.
87. Y. Feng, D. Wu, H. Li, J. Bai, Y. Hu, C. Liao, X.-y. Li and K. Shih, *ACS Sustainable Chem. Eng.*, 2018, **6**, 3624-3631.
88. S. S. Shinde, M. P. Hay, A. V. Patterson, W. A. Denny and R. F. Anderson, *J. Am. Chem. Soc.*, 2009, **131**, 14220-14221.
89. S. Dikalov, J. Jiang and R. P. Mason, *Free Radic. Res.*, 2005, **39**, 825-836.
90. J. M. Fontmorin, R. C. Burgos Castillo, W. Z. Tang and M. Sillanpää, *Water Res.*, 2016, **99**, 24-32.
91. L. Khachatryan and B. Dellinger, *Environ. Sci. Technol.*, 2011, **45**, 9232-9239.
92. I. Yamazaki, L. H. Piette and T. A. Grover, *J. Biol. Chem.*, 1990, **265**, 652-659.
93. H.-Y. Gao, C.-H. Huang, L. Mao, B. Shao, J. Shao, Z.-Y. Yan, M. Tang and B.-Z. Zhu, *Environ. Sci. Technol.*, 2020, **54**, 14046-14056.
94. A. Staško, M. Liptáková, F. Malík and V. Mišík, *Appl. Magn. Reson.*, 2002, **22**, 101-113.
95. Y. Li, Y. Pan, L. Lian, S. Yan, W. Song and X. Yang, *Water Res.*, 2017, **109**, 266-273.
96. W. Li, X. Zhang and J. Han, *Environ. Sci. Technol.*, 2022, **56**, 16929-16939.
97. J. Lu, Q. Huang and L. Mao, *Environ. Sci. Technol.*, 2009, **43**, 7062-7067.
98. S.-H. Chung, G. H. Park, N. Schukkink, H. Lee and N. R. Shiju, *Chem. Commun.*, 2023, **59**, 756-759.
99. H. Park, T. Goto, S. Cho, H. Nishida and T. Sekino, *ACS Omega*, 2020, **5**, 21753-21761.
100. G. Li, L. Li, J. Boerio-Goates and B. F. Woodfield, *J. Am. Chem. Soc.*, 2005, **127**, 8659-8666.
101. H.-H. Kim, H. Lee, D. Lee, Y.-J. Ko, H. Woo, J. Lee, C. Lee and A. L.-T. Pham, *Environ. Sci. Technol.*, 2020, **54**, 15424-15432.

View Article Online
DOI: 10.1039/D6TA01339B

102. J. de Freitas, A. P. G. Ferreira, C. Gaglieri, G. Bannach and É. T. G. Cavalheiro, *J. Therm. Anal. Calorim.*, 2025, **150**, 4165-4176.
103. M. Mgharbel, L. Halawy, A. Milane, J. Zeaiter and W. Saad, *J. Anal. Appl. Pyrolysis*, 2023, **172**, 106014.
104. Y. Zhang, C. Causserand, P. Aimar and J. P. Cravedi, *Water Res.*, 2006, **40**, 3793-3799.
105. J. Xu, L. Wang and Y. Zhu, *Langmuir*, 2012, **28**, 8418-8425.
106. Y. J. Choe, S. H. Kim, K. Jeong and J. Kim, *Chem. Eng. J.*, 2023, **455**, 140537.

View Article Online
DOI: 10.1039/D6TA01339B

Figures

Title: Diverting the use of reduced TiO_2 from a carrier of electron-hole pairs to a reservoir of Brönsted-Lewis acidic pairs for sustainable, non-optical H_2O_2 homolysis

Authors: Minsung Kim,[1a] Gyuchan Kim,[1b] Junseo Kim,[c] Sang Hoon Kim,*[ad] Byung-Hyun Kim*[be] and Jongsik Kim*[cd]

[1] co-1st authors

* corresponding authors: kim_sh@kist.re.kr (S. H. Kim); bhkim00@hanyang.ac.kr (B.-H. Kim); jkim40@khu.ac.kr (J. Kim)

Affiliations

[a] Extreme Materials Research Center, Korea Institute of Science and Technology, Seoul, 02792, South Korea.

[b] Department of Applied Chemistry, Center for Bionano Intelligence Education and Research, Hanyang Univeristy ERICA, Ansan, 15588, South Korea.

[c] Department of Chemical Engineering (Integrated Engineering Program), Kyung Hee University, Yongin, 17104, South Korea.

[d] KHU-KIST Department of Converging Science and Technology, Kyung Hee University, Seoul, 02447, South Korea.

[e] Department of Energy and Bio Sciences, Hanyang Univeristy ERICA, Ansan, 15588, South Korea.

Table of Contents

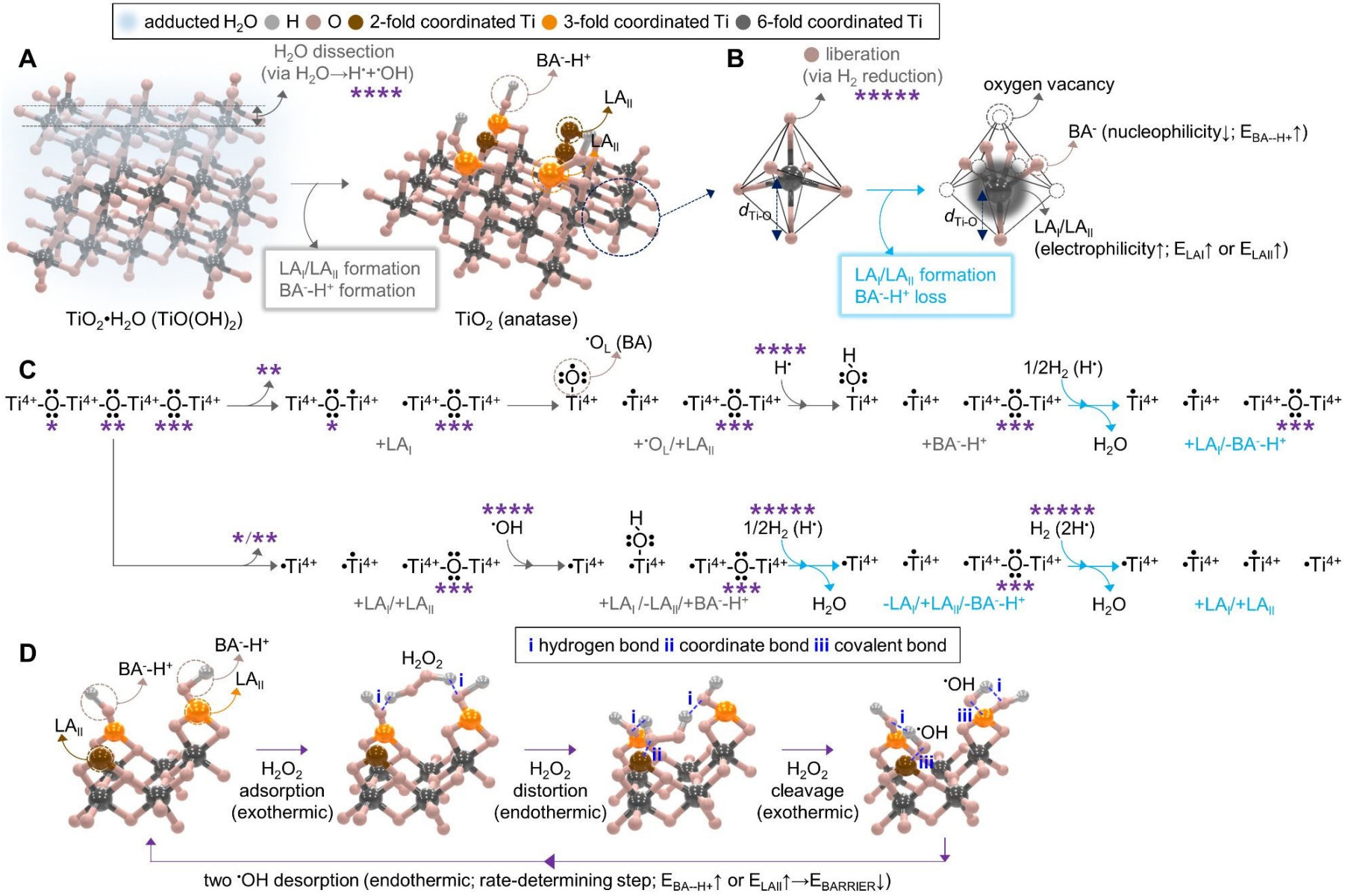

Fig. 1. (A) Illustration of *tetragonal* TiO_2 (anatase) adducted to H_2O molecules (TiO_2•H_2O), most of which undergo dissection to generate $H^•$ and $^•OH$ (****) under calcination or reduction environments. This results in the production of TiO_2 architecture, whose surfaces are terminated to bear Brönsted acidic bonds (-OH; BA^--H^+) and Lewis acidic Ti^{4+} defects with coordination numbers of 5 (LA_I) or ≤4 (LA_{II}). (B) Representation of *octahedral* TiO_2 sub-unit, where some of O^{2-} anions hexa-fold coordinated to Ti^{4+} center are released via dehydration (*****) under H_2-mediated reductive environments, making Ti^{4+} center and O^{2-} anions act as LA_I (or LA_{II}) defect and conjugate bases of BA^--H^+ bonds (BA^-), respectively. Moreover, this can also distort TiO_2 sub-unit, where Ti^{4+} center and O^{2-} anions are displaced from their original positions (*e.g.*, d_{Ti-O} reduction) and subtly alter their electronic features, thereby making Ti^{4+} center and O^{2-} anions elevate electron (e^-) affinity (E_{LAI} (or E_{LAII})↑) and deprotonation tendency (E_{BA-H+}↑), respectively. (C) Illustration of surface Ti^{4+}-O-Ti^{4+}-O-Ti^{4+}-O-Ti^{4+} channel prone to fragmentation under calcination or reduction conditions, where 1/2O_2 (*/**/***) is released, labile O ($^•O_L$) is produced and functions as BA that can be covalently bonded to $H^•$ (****), LA_I/LA_{II} are generated with LA_{II} functioning as an anchoring spot for BA^--H^+ ($^•OH$; ****), or BA^--H^+ is lost yet replaced by LA_I (or LA_{II}) via H_2-enabled dehydration. (D) Representation of elementary steps proposed to depict homolytic H_2O_2 dissection activated by BA^--H^+/LA_{II} on the terminated TiO_2 surface by way of the formation of hydrogen bond between BA^- and H of H_2O_2 (i), coordinate bond between LA_{II} and O of H_2O_2 (ii), and covalent bond between LA_{II} and O of $^•OH$ (iii), among which hydrogen (i) and covalent bonds (iii) should be weakened by elevating E_{BA-H+} and E_{LAII}, respectively, for lowering energy barrier required to proceed with the rate-determining step ($^•OH$ desorption) of catalytic H_2O_2 homolysis.

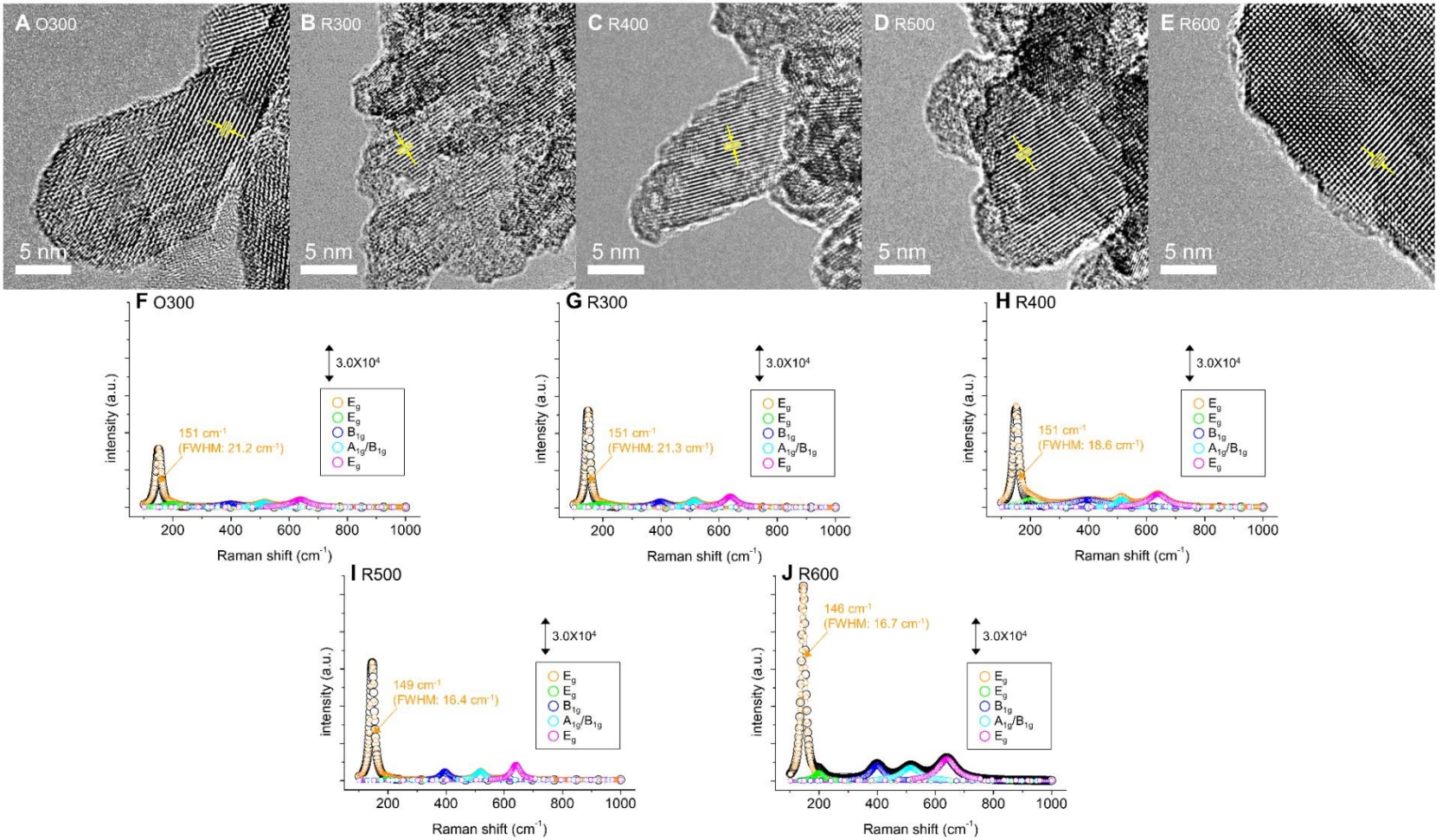

Fig. 2. HRTEM images of the catalysts (O300 for (A); R300 for (B); R400 for (C); R500 for (D); R600 for (E)), where highlighted with yellow lines and arrows are lattice fringes with *d* spacings ($d_{LATTICE}$) of 0.35 nm, which are indexed to the surface (101) facet of *tetragonal* TiO_2 (anatase; JCPDF No. of 01-071-1166). Raman spectra of the catalysts (O300 for (F); R300 for (G); R400 for (H); R500 for (I); R600 for (J)), where gray solid lines and black empty circles indicate raw spectra with the resolution of 0.5 cm^{-1} and those fitted using Lorentzian functions, respectively, whereas orange/green/blue/cyan/magenta empty circles correspond to Raman-active stretching vibrational modes for Ti^{4+}-O-Ti^{4+}-O-Ti^{4+}-O-Ti^{4+} channels belonging to *tetragonal* TiO_2 (along *a*-axis of TiO_2 lattices for E_g; along *c*-axis of TiO_2 lattices for A_{1g}/B_{1g}). Moreover, in (F-J), marked with orange arrows are E_g bands with Raman shifts centered at 146-151 cm^{-1} and their full width at half the maximum intensity (FWHM) values.

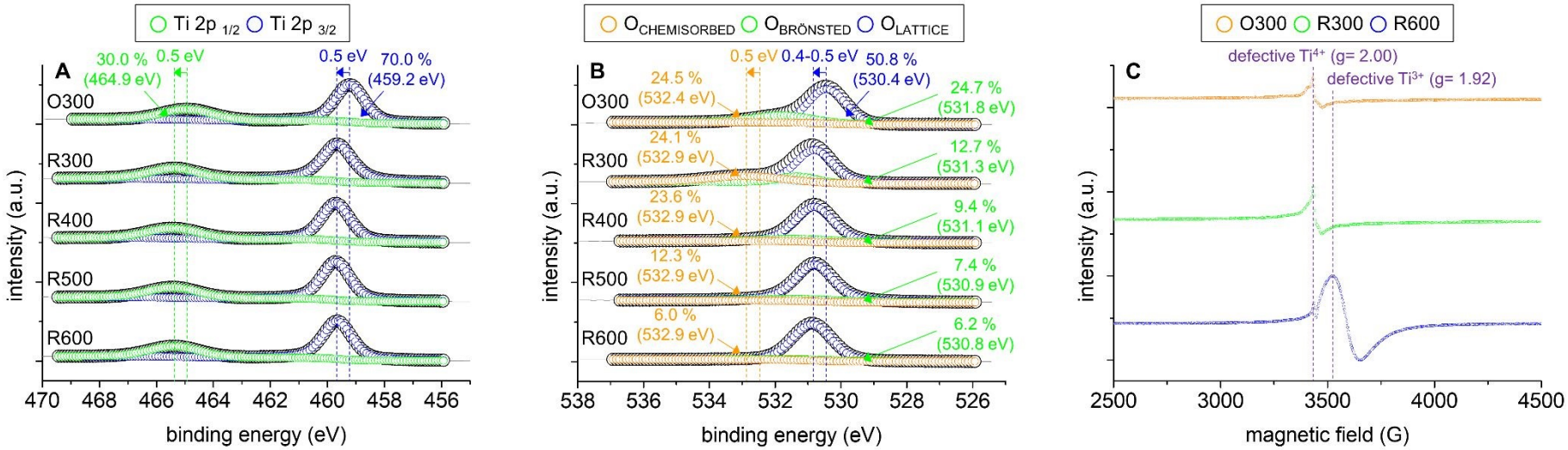

Fig. 3. XP spectra of the catalysts at the Ti 2p (A) and the O 1s regimes (B), where gray solid lines and black empty circles indicate raw spectra with the resolution of 0.05 eV and those fitted using Gaussian/Lorentzian functions, respectively. In (A), highlighted with green and blue empty circles/arrows are locations and relative concentrations of surface Ti^{4+} species belonging to the Ti 2p $_{1/2}$ and Ti 2p $_{3/2}$ regions, respectively. Moreover, in (B), highlighted with orange, green, and blue empty circles/arrows are locations and relative concentrations of O species of H_2O molecules chemisorbed on oxygen vacancies adjacent to LA_I/LA_{II} defects ($O_{CHEMISORBED}$), those of Brönsted acidic -OH bonds ($O_{BRÖNSTED}$), and those of TiO_2 lattices ($O_{LATTICE}$), respectively. EPR spectra of O300, R300, and R600 collected at 10 K, where two signals centered at g-factors of 2.00 and 1.92 stem from LA_I/LA_{II} defects (Ti^{4+}) trapping free electrons (e^-) in proximal oxygen vacancies and those (Ti^{3+}) filling their empty 3*d*/4*s* orbitals with free e^-, respectively.

View Article Online
DOI: 10.1039/D6TA01339B

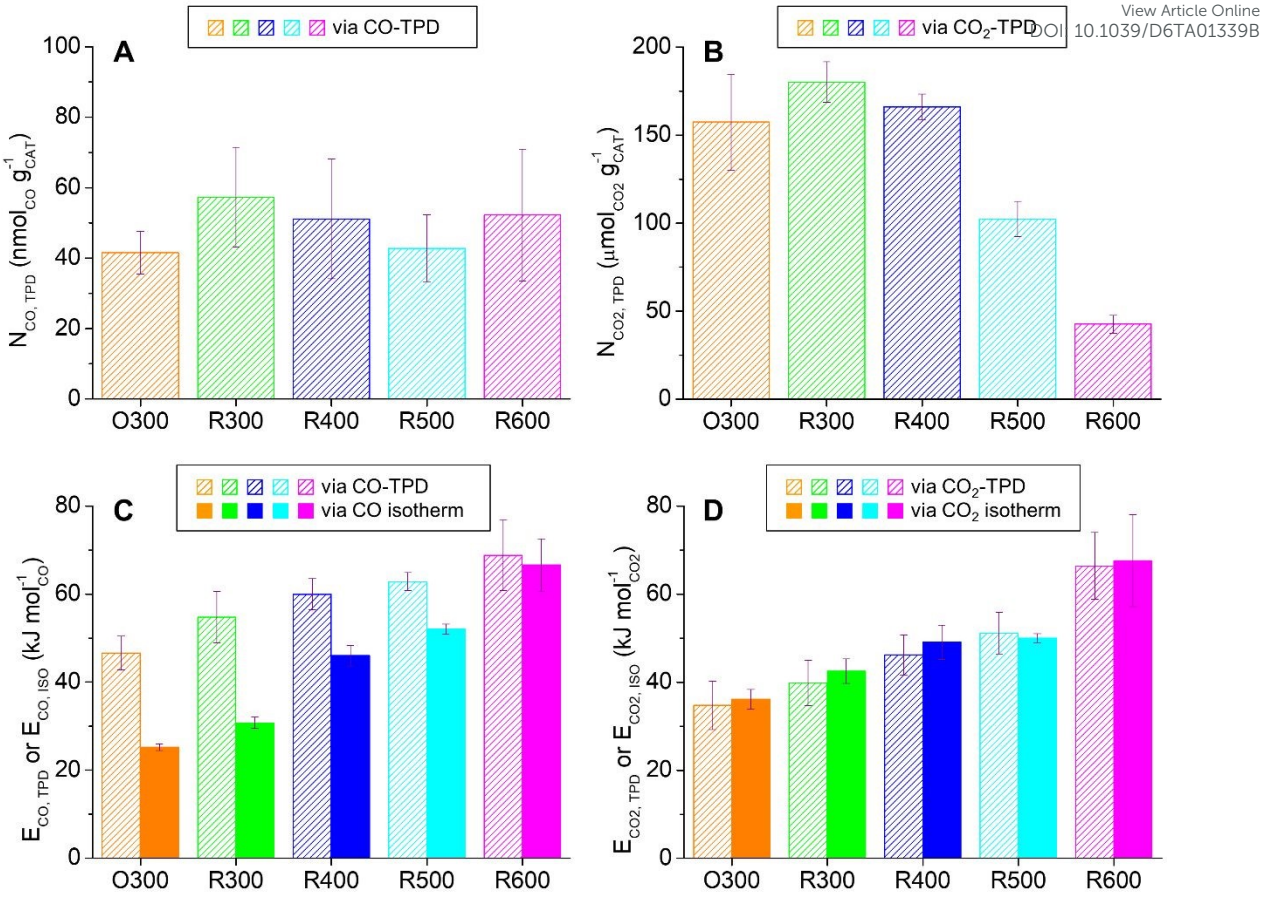

Fig. 4. The numbers of CO-accessible LA_{II} defects (A) or CO_2-accessible LA_{II} defects/BA^{-}-H^{+} bonds (B) included in a per-gram of the catalysts ($N_{CO,\ TPD}$ for A; $N_{CO2,\ TPD}$ for B) near 25 °C. Averaged CO/CO_2 binding energies of the catalyst surfaces ($E_{CO,\ TPD}$ for C; $E_{CO2,\ TPD}$ for D) and their isosteric heats of CO/CO_2 adsorption ($E_{CO,\ ISO}$ for C; $E_{CO2,\ ISO}$ for D) near 25 °C. In (A-D), $N_{CO,\ TPD}/N_{CO2,\ TPD}/E_{CO,\ TPD}/E_{CO2,\ TPD}$ values of the catalysts were assessed via CO/CO_2-TPD techniques with CO/CO_2 molecules being chemisorbed on the catalyst surfaces at 50 °C prior to their desorption, whereas $E_{CO,\ ISO}/E_{CO2,\ ISO}$ values of the catalysts were evaluated using their CO/CO_2 isotherms recorded near 25 °C.

View Article Online
DOI: 10.1039/D6TA01339B

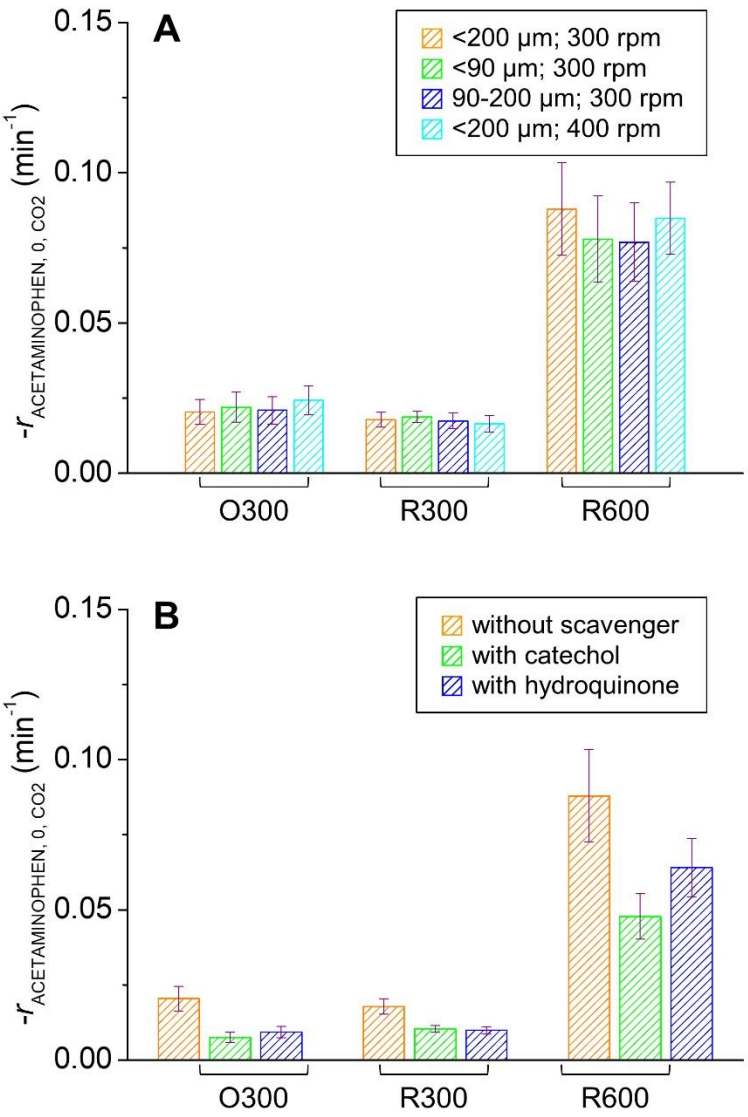

Fig. 5. Background-corrected, initial acetaminophen degradation rates normalized in a per-CO_2-accessible site basis ($-r_{ACETAMINOPHEN,\ 0,\ CO2}$) for the catalysts assessed upon the variation of catalyst particulate sizes/stirring speeds (A) or in the absence/presence of a scavenger used to quench $^{\bullet}OH/^{\bullet}OOH/O_2^{\bullet-}$ (B). Reaction environments: 0.2 g of the catalyst with sizes of <90 µm (A), 90-200 µm (A), or <200 µm (A-B); 100 mL of de-ionized H_2O; 0.1 mmol of acetaminophen; 0 mmol (A-B) or 0.82 mmol (B) of a scavenger; 0.14 mmol of Na_2SO_4; 3 V; 25 °C; 300 rpm (A-B) or 400 rpm (A); initial pH of 7.0; final pH of 4.5 (±0.3).

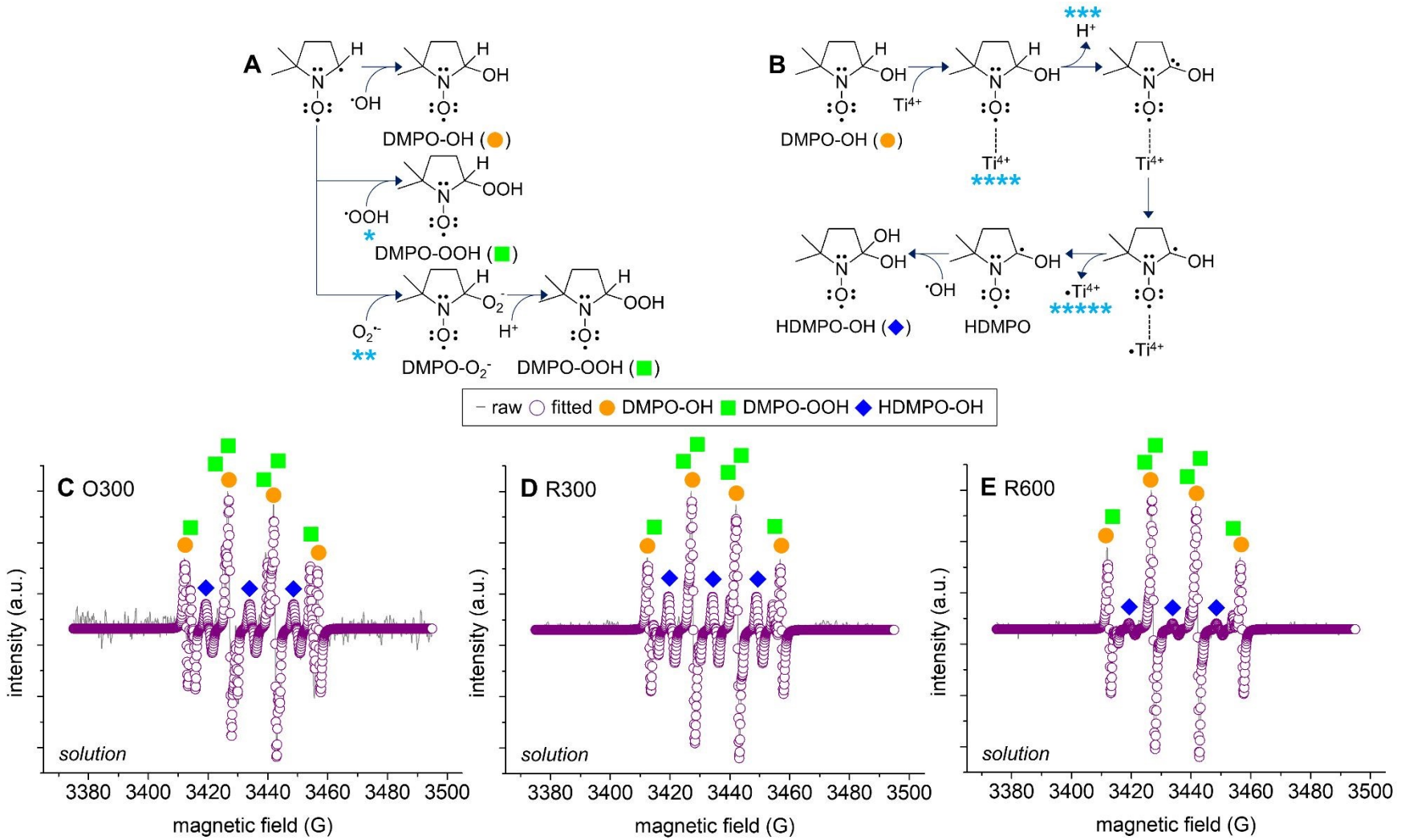

Fig. 6. (A) Depiction of formation routes for 5,5-dimethyl-1-pyrroline N-oxide (DMPO, spin trapper) species adducted to aqueous •OH (aqueous DMPO-OH) or aqueous •OOH (*)/$O_2^{\bullet-}$ (**; aqueous DMPO-OOH), for which •OH bound to BA^--H^+/LA_{II} innate to the catalyst surface should interact with aqueous H_2O_2 to generate •OOH prior to its deprotonation for transition into $O_2^{\bullet-}$ on the surface. (B) Illustration of formation route for aqueous HDMPO-OH adduct by way of aqueous DMPO-OH adsorption on

LA_{II} defect (Ti^{4+}; ****), deprotonation (***), and HDMPO desorption from •LA_{II} defect (•Ti^{4+}; *****) prior to •OH addition to aqueous HDMPO. In (A-B), •OOH formation or aqueous DMPO-OH adsorption on the surface (****) hinges on its E_{LAII} value, whereas deprotonation of •OOH or Ti^{4+}-coordinated DMPO-OH on the surface highly relies on pH value of an aqueous phase. EPR spectra of the reaction solutions collected via syringe filtration of the corresponding reaction mixtures containing H_2O, H_2O_2, DMPO, and the catalyst (O300 for (C); R300 for (D); R600 for (E)). In (C-E), gray solid lines and purple empty circles correspond to raw spectra and those simulated using Gaussian/Lorentzian functions, whereas orange solid circles, green solid squares, and blue solid diamonds are referred to as aqueous DMPO-OH, aqueous DMPO-OOH, aqueous HDMPO-OH adducts, respectively. Analytic conditions: 0.1 g of the catalyst with sizes of <200 μm; 3.0 mmol of H_2O_2; 0.2 mL of de-ionized H_2O; 0.7 mmol of DMPO; 25 °C; stirred using vortex for 2 minutes; 0.45 μm PTFE syringe filtration; final pH of 4.2 (±0.3).

View Article Online
DOI: 10.1039/D6TA01339B

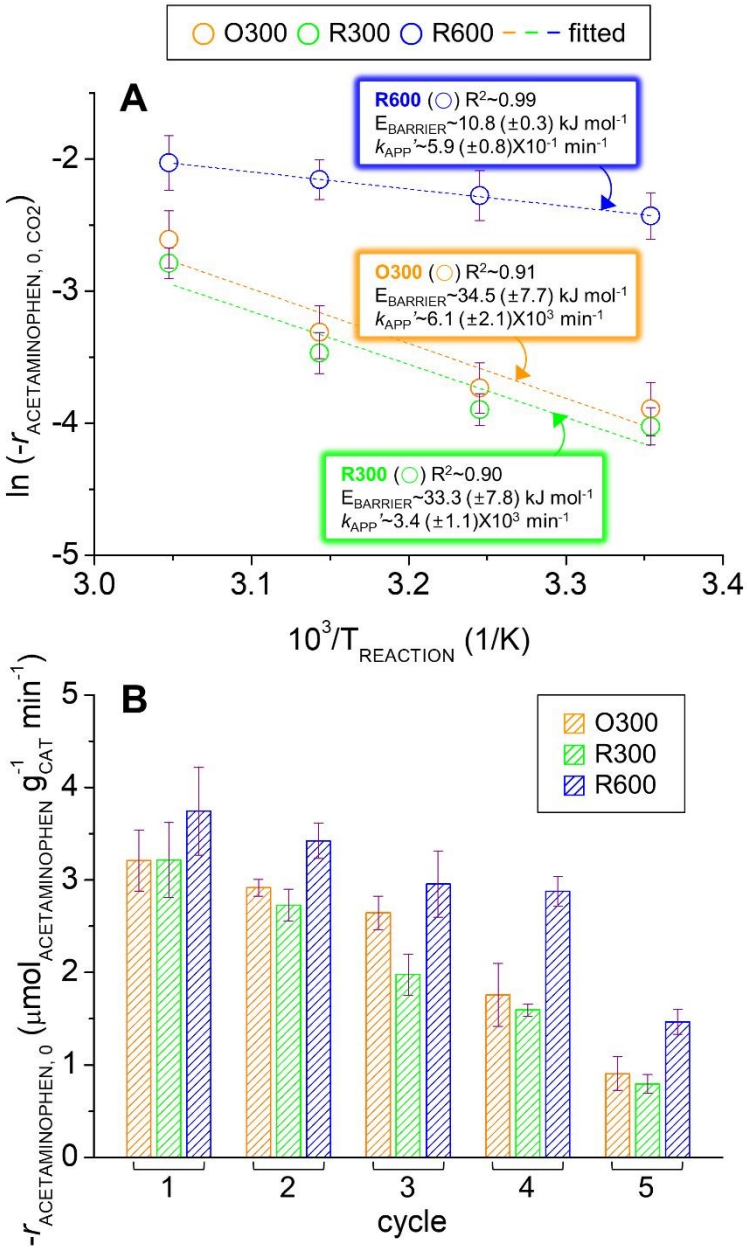

Fig. 7. (A) Arrhenius plots of logarithmic $-r_{ACETAMINOPHEN,\ 0,\ CO2}$ values (ln ($-r_{ACETAMINOPHEN,\ 0,\ CO2}$)) *versus* reciprocal of reaction temperatures ($1/T_{REACTION}$) for the catalysts, in which slopes and y-intercepts served to evaluate energy barriers ($E_{BARRIER}$) and lumped pre-factors (k_{APP}') needed to activate •OH-mediated acetaminophen degradation. (B) Background-corrected, initial acetaminophen degradation rates normalized in a per-gram basis ($-r_{ACETAMINOPHEN,\ 0}$) for the (used) catalysts subjected to acetaminophen degradation recycle runs. Reaction environments: 0.2 g of the (used) catalyst with sizes of <200 μm; 100 mL of de-ionized H_2O; 0.1 mmol of acetaminophen; 0.14 mmol of Na_2SO_4; 3 V; 25 °C (A-B) or 35-55 °C (A); 300 rpm; initial pH of 7.0; final pH of 4.5 (±0.3).

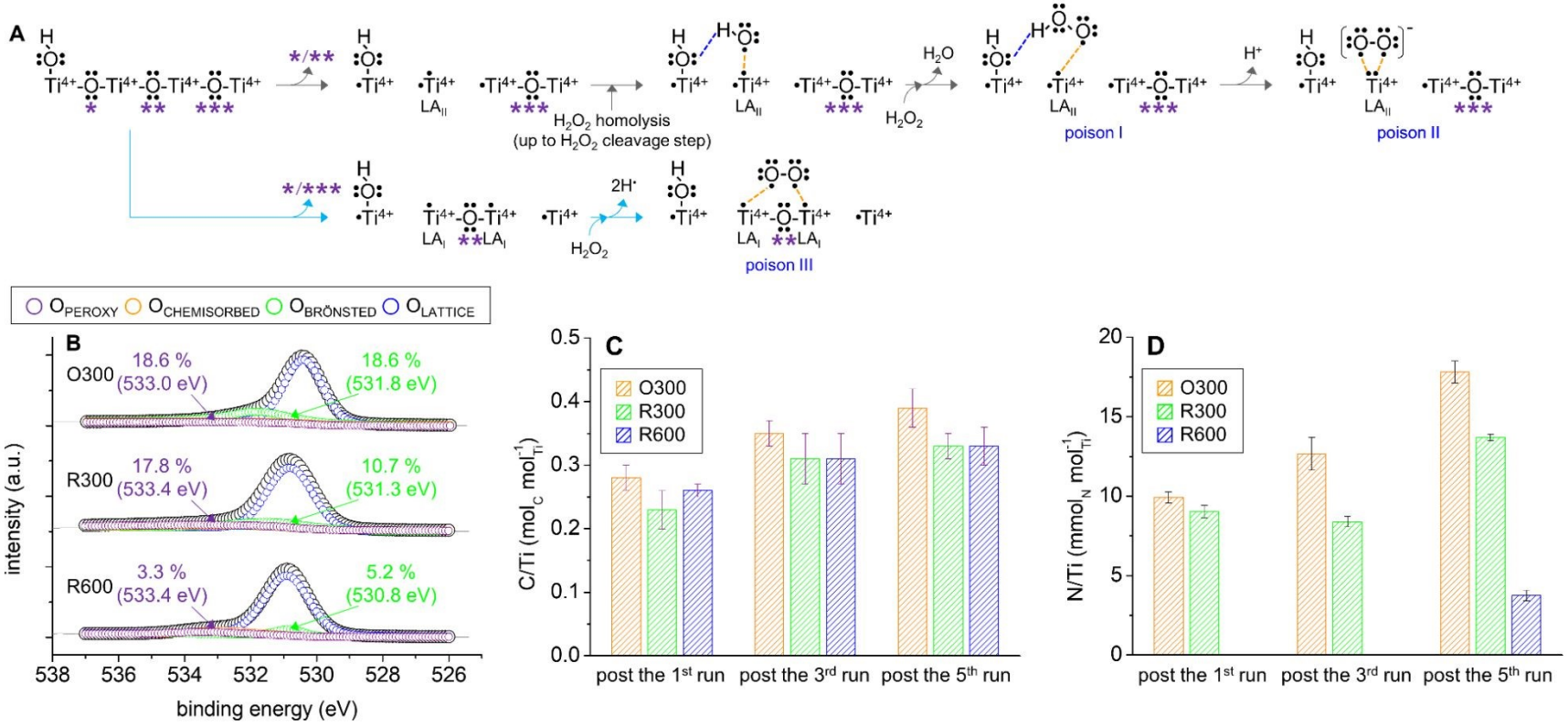

Fig. 8. (A) Depiction of BA^--H^+-modified Ti^{4+}-O-Ti^{4+}-O-Ti^{4+}-O-Ti^{4+} channel exposed to calcination or reduction environments, under which $1/2O_2$ species (*/** or */***) are released to afford LA_{II} (highlighted with gray arrows) or two LA_I defects (highlighted with skyblue arrows). In (A), BA^--H^+ and LA_{II} can serve to activate H_2O_2 homolysis up to H_2O_2 cleavage step, upon which $^{\bullet}OH$ bound to BA^--H^+/LA_{II} can potentially undergo transition to surface $^{\bullet}OOH$ (poison I) and $O_2^{\bullet-}$ (poison II) via interaction with aqueous H_2O_2 and deprotonation, respectively (highlighted with gray arrows), in lieu of being released to an aqueous phase via desorption. Moreover, in (A), two LA_I defects can tentatively interact with aqueous H_2O_2, liberate two $H^{\bullet}$ species, and covalently bind with O_2 (poison III), as highlighted with skyblue arrows. (B) XP spectra of the homolytic H_2O_2 dissection-subjected catalysts in the O 1s regimes, where gray solid lines and black empty circles indicate raw spectra and those fitted using Gaussian/Lorentzian functions with the resolution of 0.05 eV. In (B), purple, orange, green, and blue empty circles indicate $^{\bullet}OOH/O_2^{\bullet-}/O_2$ (poison I/II/III; O_{PEROXY}), $O_{CHEMISORBED}$, $O_{BRÖNSTED}$, and $O_{LATTICE}$, respectively, among which locations and relative concentrations of O_{PEROXY} and $O_{BRÖNSTED}$ are highlighted with purple and green arrows, respectively. Atomic ratios of C to Ti (C/Ti; C) or N to Ti (N/Ti; D) included in the (used) catalysts subjected to acetaminophen degradation recycle runs. Reaction environments: 0.2 g of the (used) catalyst with sizes of <200 μm; 100 mL of de-ionized H_2O; 0.1 mmol of acetaminophen; 0.14 mmol of Na_2SO_4; 3 V; 25 °C; 300 rpm; initial pH of 7.0; final pH of 4.5 (±0.3).

View Article Online
DOI: 10.1039/D6TA01339B

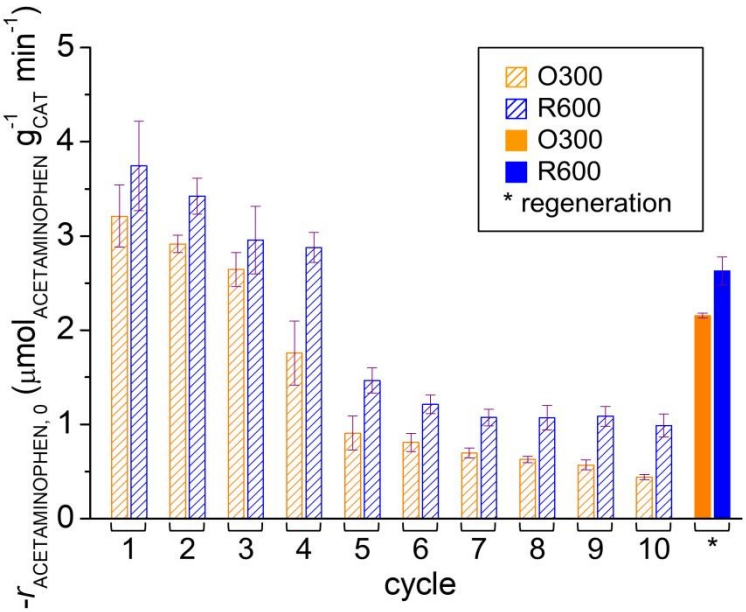

Fig. 9. Background-corrected, initial acetaminophen degradation rates normalized in a per-gram basis ($-r_{ACETAMINOPHEN,\ 0}$) for (used) O300 and R600 subjected to acetaminophen degradation recycle runs and $-r_{ACETAMINOPHEN,\ 0}$ values for O300 and R600 subjected to the 10th cycle of acetaminophen degradation recycle runs followed by regeneration (marked with *). Reaction environments: 0.2 g of the (used or regenerated) catalyst with sizes of <200 μm; 100 mL of de-ionized H_2O; 0.1 mmol of acetaminophen; 0.14 mmol of Na_2SO_4; 3 V; 25 °C; 300 rpm; initial pH of 7.0; final pH of 4.5 (±0.3). Regeneration conditions: under a N_2; ramping rate of 5 °C min^{-1}; 300 °C; 4 hours.

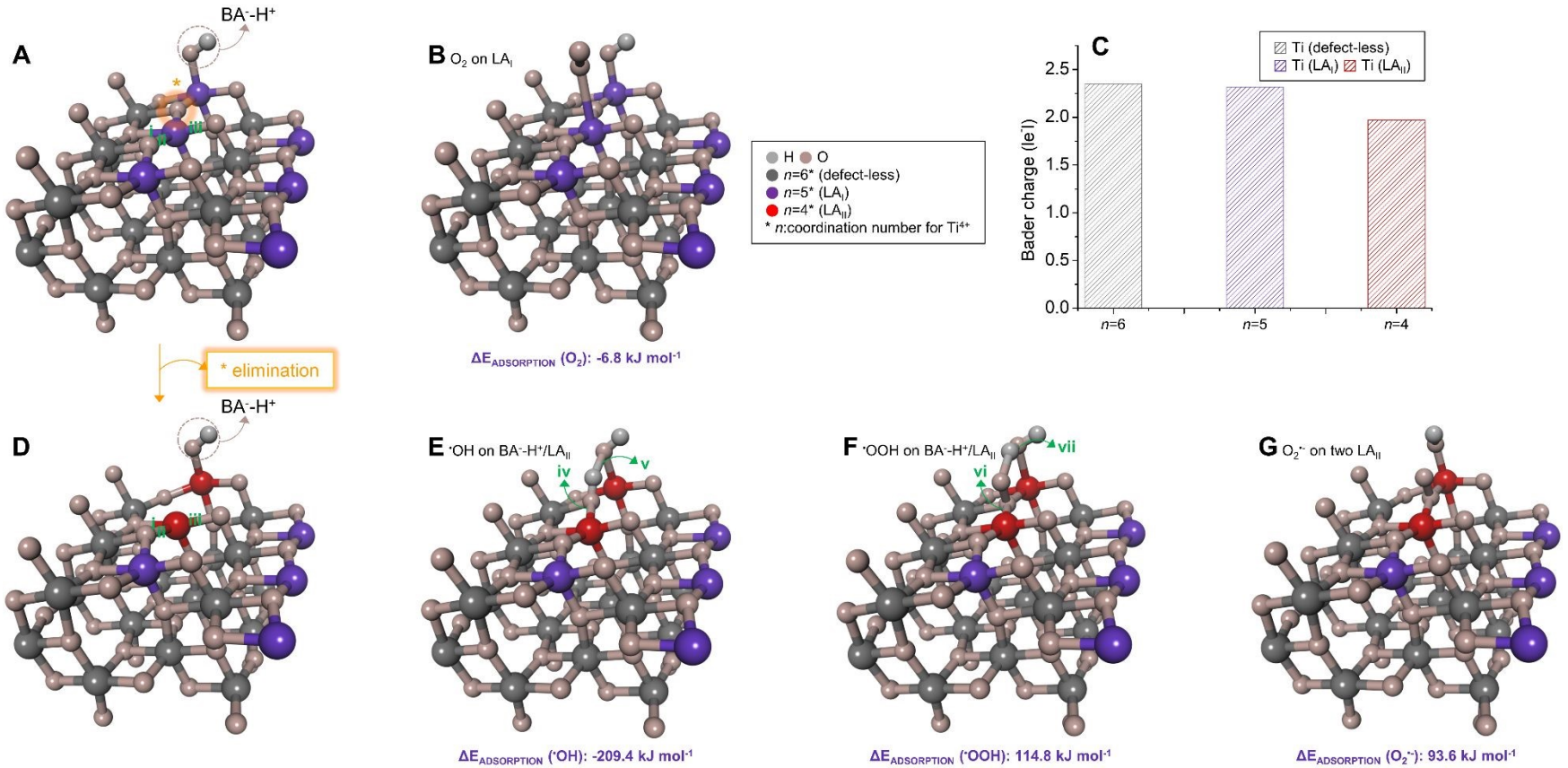

Fig. 10. Representation of *tetragonal* TiO_2 (anatase) slab subjected to termination on its (101) facet followed by geometric optimization (A; denoted as surface I), upon which 5-fold coordinated Ti atoms (LA_I) and BA^--H^+ were imparted, whereas O atom marked with * was eliminated for transition of vicinal LA_I sites to 4-fold coordinated Ti analogues (LA_{II}; D; denoted as surface II). Bond lengths marked with i, ii, and iii were computed to be 2.06 Å, 2.00 Å, and 1.86 Å, respectively, for the surface I (A), whereas those were calculated to be 2.04 Å, 1.96 Å, and 1.88 Å, respectively, for the surface II (D). (C) Bader charges of 4/5/6-fold coordinated Ti atoms pertaining to the surface II. Depiction of the surface I adsorbing O_2 on LA_I (B) in addition to the change in thermodynamic energy involved in O_2 adsorption on the surface I ($\Delta E_{ADSORPTION}$ (O_2)). Illustration of the surface II adsorbing $^{\bullet}OH$ on BA^--H^+/LA_{II} (E), $^{\bullet}OOH$ on BA^--H^+/LA_{II} (F), or $O_2^{\bullet-}$ on two LA_{II} (G) alongside with the change in thermodynamic energy involved in $^{\bullet}OH$, $^{\bullet}OOH$, or $O_2^{\bullet-}$ adsorption on the surface II ($\Delta E_{ADSORPTION}$ ($^{\bullet}OH$), $\Delta E_{ADSORPTION}$ ($^{\bullet}OOH$), or $\Delta E_{ADSORPTION}$ ($O_2^{\bullet-}$)). Bond lengths marked with iv and v were computed to be 2.05 Å and 1.61 Å, respectively, for the surface II (E), whereas those marked with vi and vii were calculated to be 2.10 Å and 1.01 Å, respectively, for the surface II (F).

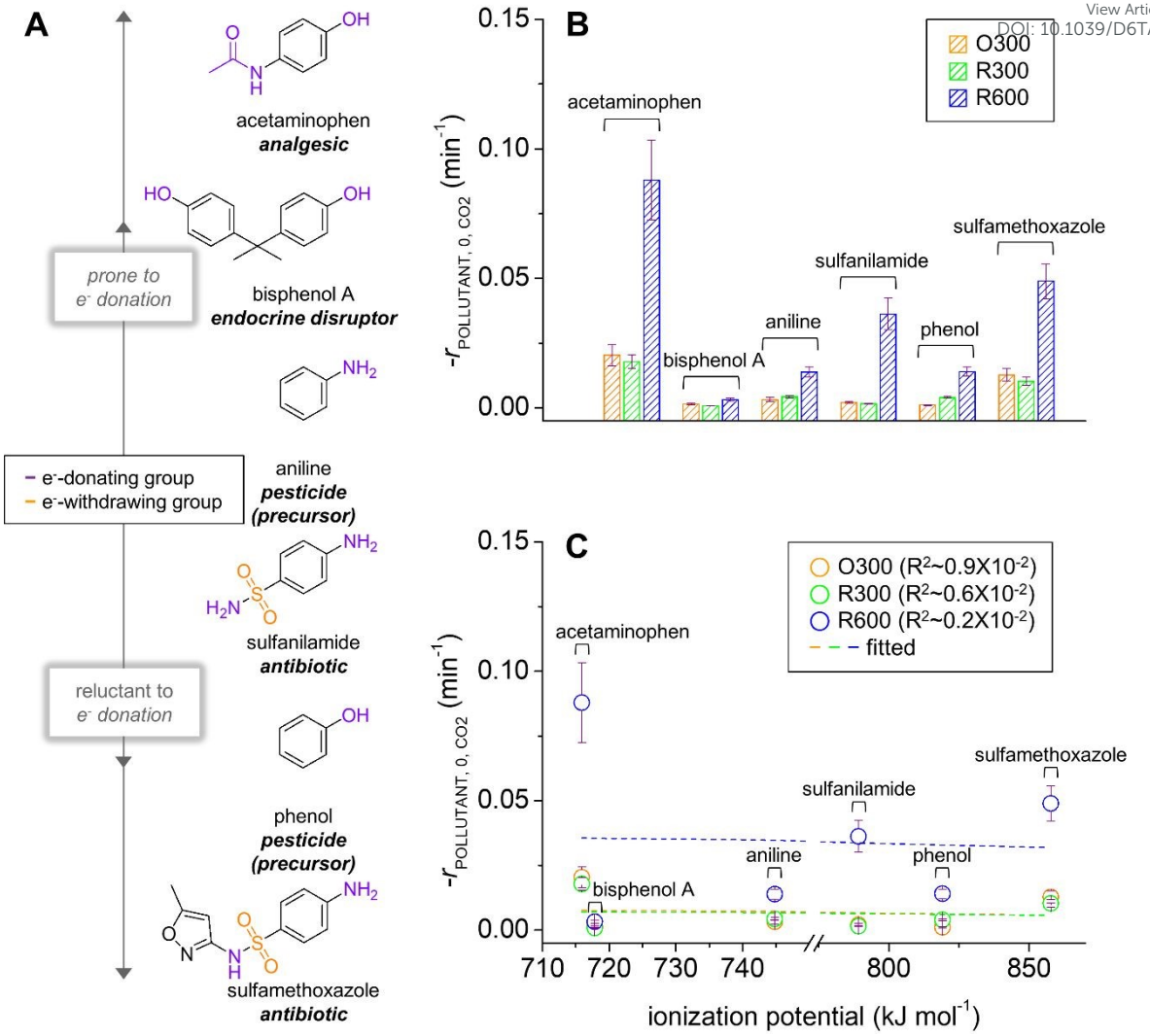

Fig. 11. (A) Model compounds of hard-to-fragment, aqueous pollutants with distinct electronic features with regard to e^- donation/acceptance or ionization tendency. (B) Background-corrected, initial pollutant degradation rates normalized in a per-CO_2-accessible site basis ($-r_{POLLUTANT,\ 0,\ CO2}$) for the catalysts and (C) their plots of $-r_{POLLUTANT,\ 0,\ CO2}$ values *versus* ionization potentials of pollutants. In (C), shown with dashed lines are the fits of the plots, across which their regression factors (R^2) were evaluated. Reaction environments: 0.2 g of the catalyst with sizes of <200 μm; 100 mL of de-ionized H_2O; 0.1 mmol of acetaminophen, 0.1 mmol of aniline, 0.1 mmol of sulfanilamide, 0.1 mmol of phenol, 0.1 mmol of sulfamethoxazole, or 0.004 mmol of bisphenol A; 0.14 mmol of Na_2SO_4; 3 V; 25 °C; 300 rpm; initial pH of 7.0; final pH of 4.5 (±0.3).

View Article Online
DOI: 10.1039/D6TA01339B

Data availability Statement

The data supporting this article have been included as part of the Supplementary Information.